Designing a SODAR testbed for RADAR applications

By

Zeus Edgar Gannon
B.S., University of Kansas, 2019

Submitted to the graduate degree program in Electrical Engineering and Computer Science and the Graduate Faculty of the University of Kansas in partial fulfillment of the requirements for the degree of Master of Science.

Chair: Dr. Christopher Allen

Dr. Shannon Blunt

Dr. James Stiles

Date Defended: 10 December 2021

The thesis committee for Zeus Edgar Gannon certifies that this is
the approved version of the following thesis:

Designing a SODAR testbed for RADAR applications

Co-Chair: Dr. Christopher Allen

Co-Chair: Dr. Shannon Blunt

Co-Chair: Dr. James Stiles

Date Approved: 10 December 2021

Abstract

In research there exists a need to constantly test and develop systems. Testing a radar system requires costly resources in terms of equipment and spectrum. These challenges relegate most testing to simulations, which are a poor approximation of reality. An alternative to over-the-air radar testing is presented here in the form of an over-the-air ultrasonic detection and ranging (SODAR) system. This system takes advantage of the similar wave-like propagation properties of acoustic and electromagnetic waves. With a sodar testbed, radar waveform design can quickly move out of simulation and into the real world with minimal overhead. In this thesis, basic and advanced radar sensing are demonstrated with a sodar setup. Range detection, Doppler sensing, and pulse compression are shown as examples of basic radar concepts. These basic radar tests prove that the fundamentals of radar also work with a SODAR setup. For advanced sensing applications, array-based direction finding and synthetic aperture radar (SAR) are shown. The direction-finding portion resolves three separate transmission sources with an 8-channel array. The thesis continues with a demonstration of SAR collections on multiple objects and culminates with a SAR image of a complex small-scale vehicle.

Acknowledgments

I'd like to thank Stephanie and Lita for their continual love and support during this endeavor. I'd also like to thank Dr. Christopher Allen for being my advisor and mentor during my graduate education. Thanks to the RSL staff and students for fostering a productive lab environment including Dr. Shannon Blunt, Dr. James Stiles, Roger Williams, Christian Jones, Daniel Herr, and Brandon Ravenscroft. I'd like to acknowledge Dr. Alessandro Salandrino and Dr. Ken Demarest for proving me with a strong foundation in electromagnetics. I would also like to give a big thank you to Tom Colwell at the EECS shop for letting me constantly borrow parts and equipment needed to get my experiments running.

Table of Contents

List of Figures

1 Introduction

Radar is a very developed field of sensing spanning almost 90 years. Early radar systems consisted of entirely analog components and required artful manipulation of physics in order to detect an object. These early systems required massive dedicated facilities and trained engineers to maintain. In contrast, modern radar systems are almost entirely digital. A system operating under 4 GHz can consist of an antenna connected directly to a digital converter, which passes the samples on for digital signal processing. These systems are small enough to fit into a watch. Radar research involves having custom built equipment that is much larger and more difficult to maintain than purpose-built consumer systems.

There exists well developed theory about EM waves and radar, why explore this same phenomenon in the acoustic domain? One of the reasons is cost. To get together all of the equipment and test facilities to perform a single radar measurement can take weeks of planning and thousands of dollars. A sodar setup costs on the order of dollars for transmission equipment and can be setup quickly. The reduced cost allows for design and experimentation by institutions or individuals that don't have a large budget. This can help move radar waveform design and general remote sensing into the hands of community colleges and perhaps high schools.

A sodar setup also serves as an important step between simulation and full RF experimentation. Simulation does not include many of the realities of an actual experiment. However, in transition to an experiment all of the realities are added in at once. If the experiment doesn't work as intended, it can be difficult to determine the cause. With this intermediate step, some realities can be included while others can be left out. For instance, making a clutter and multipath free environment for acoustic waves is much easier than in RF. Having an object

produce a Doppler signature without moving would be impossible if not in simulation or with an "active target." In the acoustic domain this behavior can be obtained with a simple tuning fork.

A sodar setup also brings the experiment's size down to that of a laboratory. Not having to reserve space outdoors for a test or consult the FCC spectrum allocation chart means that a test can be carried out in an afternoon without much if any planning. This short setup time also allows for quick iterations on waveform design. Once testing is done the data can be immediately offloaded onto a processing computer without having to wait for an orbital data link or offloading of a plane. The data can then be processed, analyzed, adjusted, and then put back into the test system in the same afternoon rather than having to schedule another flight or reserve time on the range.

Chapter 2 reviews the relevant theory from the perspective of its original derivation, radio waves. The physical wave interactions are first presented. These topics include range, range resolution, Doppler, Doppler resolution and antenna contributions. Processing techniques are then outlined. This includes pulse compression, coherent averaging, and windowing.

Chapter 3 covers the equipment used. The transmitters and receivers are first discussed. Secondly, the waveform generation equipment and recording equipment are described. Each of these sections also include important features that aid in testing or than enable the testing in the first place. The objects used in testing, two trihedrals, are covered last.

Chapter 4 details the experiments that were performed. First the basic radar experiments show that the SODAR testbed accurately recreates the phenomenology seen in radar systems. Lastly, two examples of advanced radar sensing are demonstrated. These represent useful setups that could further research for a paper or project.

2 Theory

2.1 Basic Radar Concepts

2.1.1 Range and Range Resolution

Once an EM wave is launched it propagates at the speed of light in the media. In a vacuum this is the speed of light, 2.99792 * 10^8 m/s. In media with a relative dielectric constant higher than one, the speed of light is reduced. For purposes here, the media of propagation will be free space, which has a relative dielectric constant of one. As the wave propagates it will reflect off objects in its path. If a portion of the reflected wave is received by the same device that launched the wave, the round-trip travel time T can be measured. This is referred to as a colocated transmitter and receiver. From this knowledge and the speed of propagation, c, the range of the object, R, can be determined.

$$R = \frac{c\,T}{2}\ (meters)$$

A system that performs radio detection and ranging is commonly referred to as a RADAR. Radio waves are EM waves with a wavelength greater than infrared. Currently, the shortest wavelengths that conventional radar operates is in the millimeter range. The radio spectrum is further divided into different sub bands based on convention. The wavelength of the EM wave being used also imposes limits on the system hardware that will be covered later.

As the EM wave travels in the media from its origin point, it does so in a spherical wave. Only a portion of this wave is reflected back to the receiver, and this reflected wave also propagates in a spherical wave. This loss of energy is referred to as spherical spreading loss or free space transmission loss. This can be described with the following equation.

$$P_R = \frac{P_T}{(4\,\pi\,R^2)^2}$$

Where P_R is the received power, P_T is the transmitted power, and R is the range to the object. There is no way to avoid this loss. However, there are devices that can drastically increase the transmitted power which will be covered later. If a signal's power becomes too weak, it will be immersed in noise and unrecoverable without signal post-processing.

Most scenes include more than one object. The ability of the radar to discriminate between multiple objects in range is referred to as range resolution ΔR. Radar systems commonly operate in a pulsed mode, and the duration of this pulse τ is directly related to the range resolution. A simple example of this relation is shown in Figure 1:

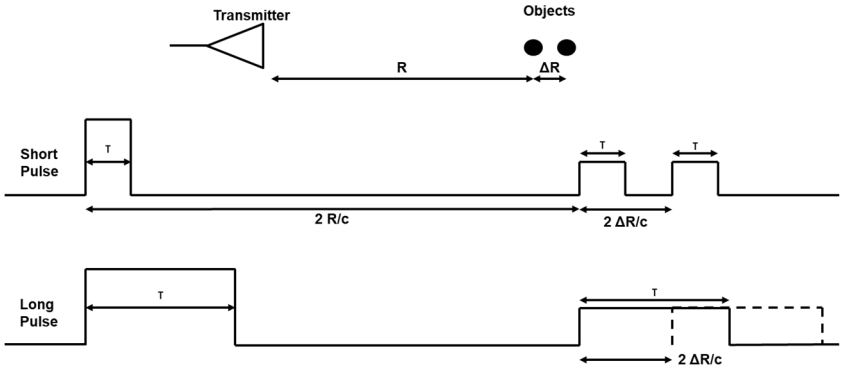

Figure 1: Range Resolution Example

The simplest waveform a pulsed radar can transmit is a gated sinusoid. As the pulse shortens it becomes easier to resolve targets, but it becomes harder to produce the power levels required to overcome the free space loss. In order to resolve the objects, the pulse length must be shorter than the round-trip propagation time between the two objects.

$$\tau \leq \frac{2\,\Delta R}{c}\ (seconds)$$

This can be rearranged to better show the definition of range resolution.

$$\Delta R = \frac{c\,\tau}{2}\ (meters)$$

Another way to describe the benefit of a shorter pulse is to examine pulses in both the time and frequency domains. The shorter pulse has a much wider spectral bandwidth than the longer pulse as shown in the following example.

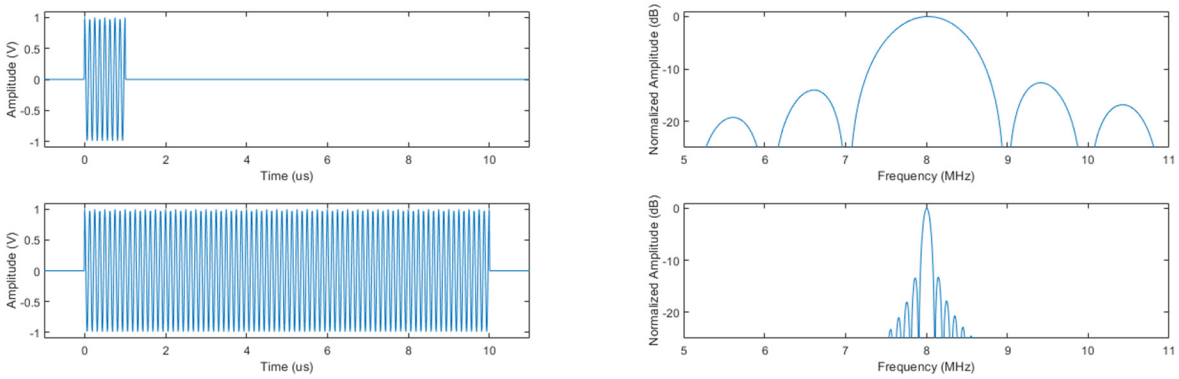

Figure 2: A 1 us pulse (top) and a 10 us pulse (bottom) of an 8 MHz sinusoid

If the extended bandwidth causes the finer range resolution, then using a shorter pulse should prove better than a longer one. The limiting factor in this case becomes the hardware used to generate the pulse. However, there are other ways to fill a constant time window with more bandwidth that will be covered later. Range resolution using the 3 dB bandwidth, B, of this gated sinusoid signal can be describes as follows.

$$\Delta R = \frac{c}{2\,B}\,, where\ B = \frac{1}{\tau}$$

2.1.2 Doppler and Doppler Resolution

If a propagating EM wave interreacts with a non-stationary object, there is a transfer of momentum. If the object is moving towards or away from the radar this momentum change can be detected. When an object that is moving towards the radar encounters an EM wave, it transfers some of its momentum into the wave. Since the EM wave cannot increase in speed, it instead increases in frequency. An EM wave encountering an object moving away from the radar will have some of its momentum transferred into the object. This results in a lower energy and

thus lower frequency wave being received by the radar. This change in frequency, known as the Doppler effect, is proportional to the radial velocity of the object as shown.

$$f_D = \frac{2\,v_r}{\lambda}\ (Hertz)$$

Where v_r is the radial velocity approaching the radar and λ is the wavelength of the transmitted signal. In the time domain this effect appears as a phase compression or decompression. In the frequency domain the peak of the returned signal is shifted higher or lower by the Doppler frequency.

If the radar encounters two objects moving at different radial (coming towards or moving away) velocities, the ability to distinguish between those frequencies is known as Doppler resolution. As is common in Fourier analysis, the longer the observation time, *t*, the finer the frequency resolution. This results in pulse length requirements of one second in order to achieve a resolution of one Hertz.

$$\Delta f_D = \frac{1}{t}\ (Hertz)$$

Where Δf_D is the Doppler resolution in Hz and *t* is the observation time in seconds.

2.1.3 Pulse Compression

There is already an evident engineering trade-off between range resolution, Doppler resolution, and energy on the object. Doppler resolution and energy on object benefit from increased pulse durations, while range resolution benefits from short durations. However, the range resolution dependence can also be described using the concept of spectral bandwidth. There does exist a method to keep long pulse durations while increasing the spectral bandwidth of a signal, and that is pulse compression.

The most straightforward way of adding bandwidth to a signal is to chirp it. A chirp is a sweeping tone that transitions from one frequency to another over the pulse duration. The

frequency/time slope further defines the type of chip. The most common is a linear sweep and has been coined the linear frequency modulated chirp (LFM). The time domain representation is as follows.

$$s(t) = A\cos\left(2\pi\left(f_c\,t + \frac{B}{\tau}\,t^2\right) + \phi_c\right),\ where\ 0 \le t \le \tau$$

Where A is the amplitude of the signal, f_c is the starting frequency, B is the desired bandwidth, τ is the pulse duration, and ϕ_c is the initial phase offset.

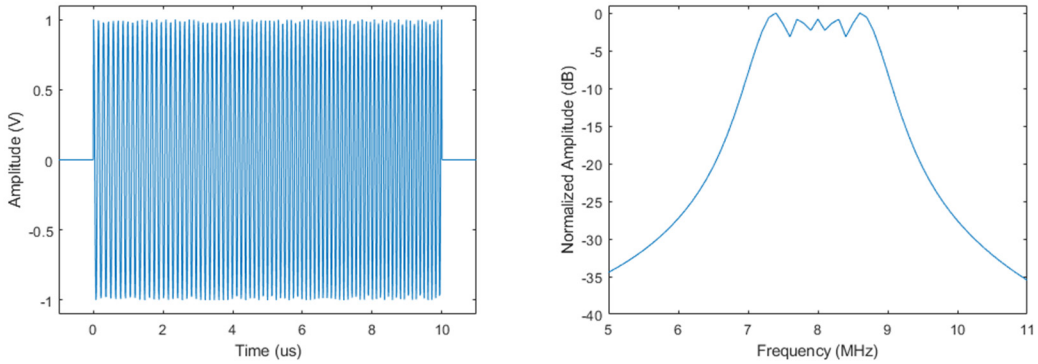

Figure 3: A 10 us chirped sinusoid with a center frequency of 8 MHz and 2 MHz of 3 dB bandwidth

As seen in the figure, when compared to the 10 us sinusoid, the LFM has significantly wider 3 dB bandwidth. This enables the waveform to maintain a fine Doppler resolution and allows for a fine range resolution. As the only downside is slightly increased transmitter complexity and receiver processing, it's clear to see why the LFM waveform has become ubiquitous with radar systems.

2.1.4 Windowing

Using an LFM for the transmit signal requires a different type of receive processing to utilize the increased bandwidth. The received signal must be correlated with the transmit signal to reveal object detection. Since time-domain correlation is processing intensive, this is usually

done as multiplication in the frequency domain using the fast Fourier transform (FFT). The correlation process results in range sidelobes in addition to the main return. This can be improved with different windowing functions for the FFT. This tapers the leading and trailing edges of the convolution at the heart of the FFT. This can result in a reduction of the sidelobes in the processed return.

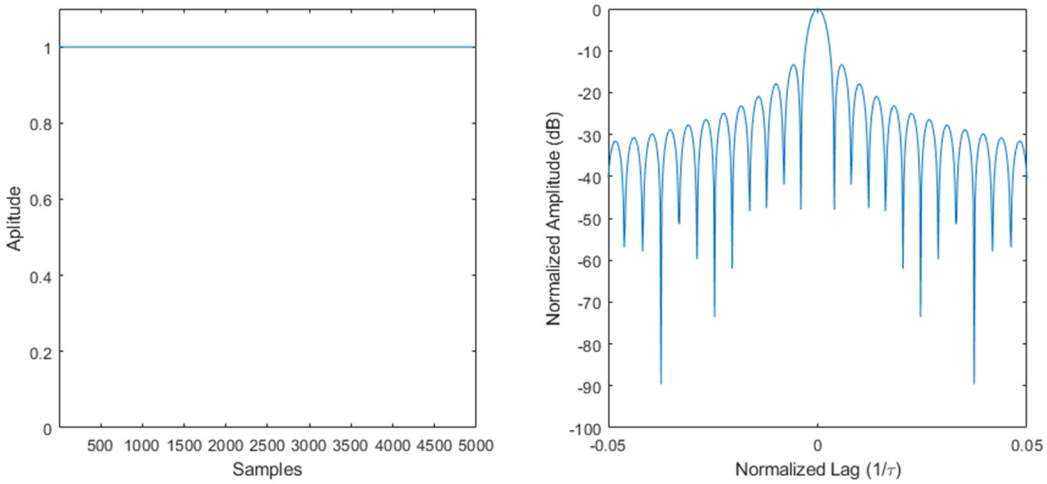

Figure 4: The rectangular windowing function applied to an LFM correlation function

This is the standard windowing function and serves as a baseline to demonstrate improvement.

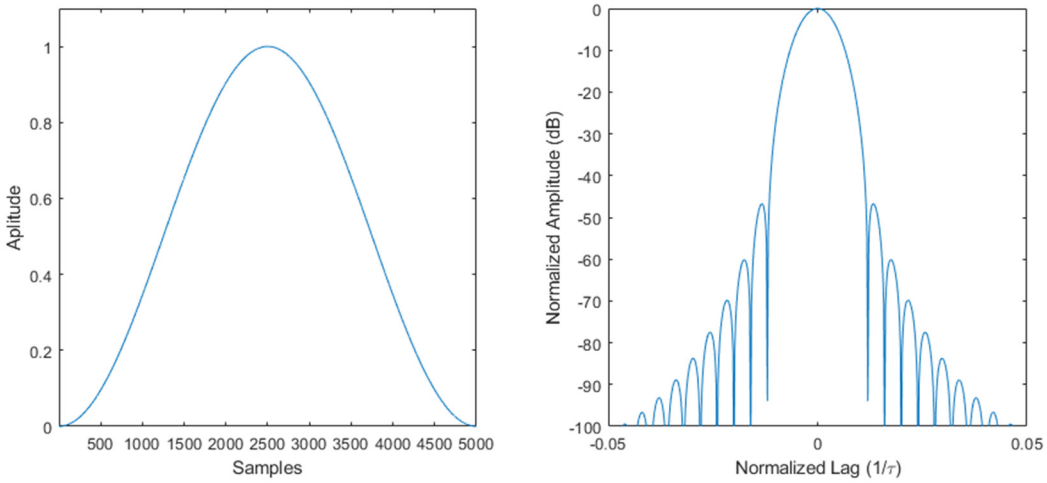

Figure 5: The Hanning windowing function applied to an LFM correlation function

The Hanning window drives down the range sidelobes much farther than the rectangular window. However, removing the edge frequency components results in a loss of sharpness in the 3 dB main lobe.

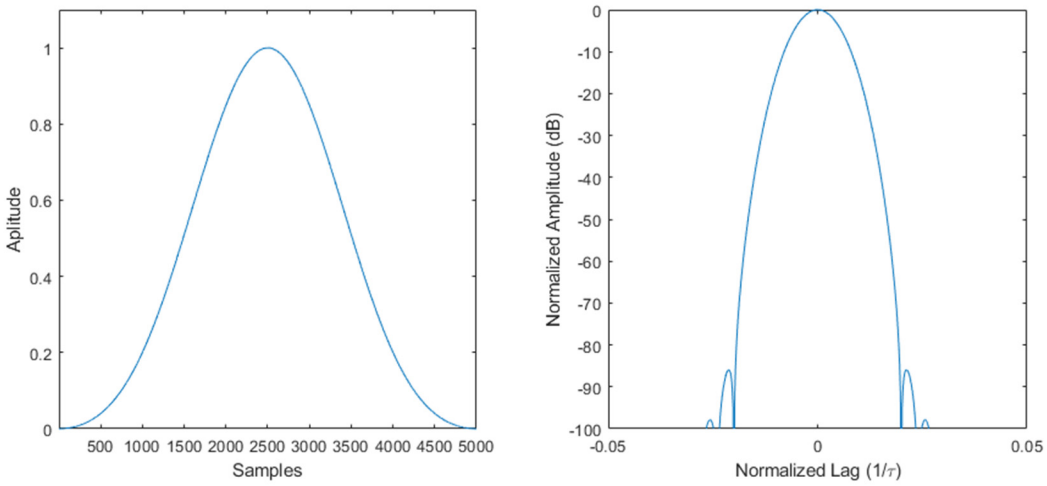

Figure 6: The Blackman-Harris windowing function applied to an LFM correlation function

The Blackman-Harris window offers even better sidelobe suppression, but at the cost of a much wider main lobe.

2.1.5 Coherent Averaging

Along with the returned signal there is the ever-present component of random noise. In the frequency domain noise manifests as a low power amplitude randomness across all frequencies. Many signal returns can be averaged together in a process known as coherent averaging. This averaging occurs on a pulse to pulse basis, also known as slow time. Since noise is a random process, as the coherent signals are added together the average noise power decreases due to the noise signal being incoherent. This can be shown in the frequency domain as a lowering of the average noise power or noise floor. Intra-pulse (fast time) coherent averaging is also possible if fast-time the sample rate is significantly higher than the highest frequency in the waveform.

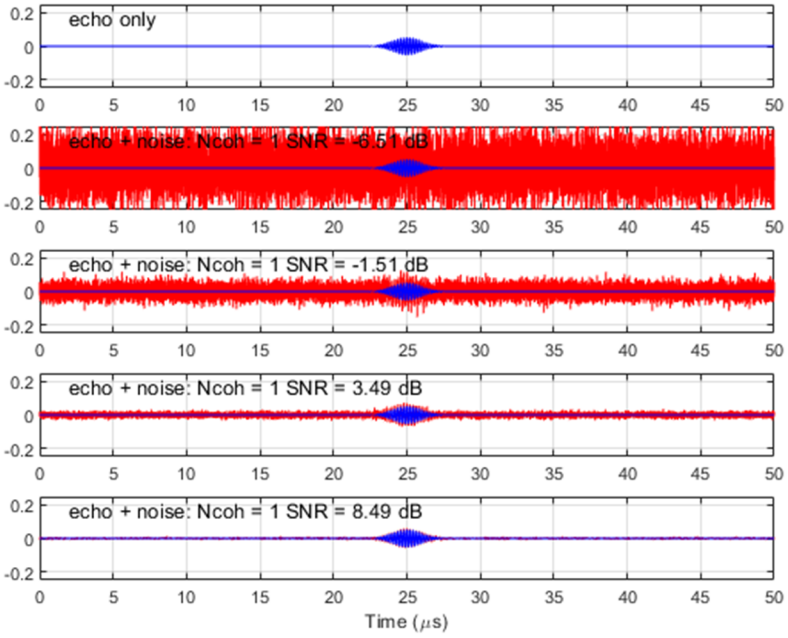

Figure 7: A pulsed signal with 1, 10, 100, and 1000 integrations

The number of coherent integrations N_{coh}has a multiplicative improvement on the power received from a transmitter. If there are 10 integrations, then the received signal is 10 times greater than it would have been without the integrations. This effect is shown in a modification to the equation presented in the noise section.

$$P_R = \frac{P_T\, N_{coh}}{(4\,\pi\, R^2)^2}$$

2.1.6 Antennas and Gain

In order to get the EM wave out of the circuitry and into the air it must go through an antenna. These devices also serve as spatial, spectral, and polarization discriminators depending on their physical size and the wavelength of the EM wave they transmit. Their property that translates best into the acoustic domain is focusing energy in a particular direction. Instead of transmitting isotopically (in all directions equally), a directional antenna will focus a beam usually less than 45°. As this angle decreases the power in that direction compared to an

isotropic radiator, or gain, will increase. Both the gain of the transmitter G_T antenna and receiver G_R antenna contribute to the increase in received power as can be seen in the following equation.

$$P_R = \frac{P_T\, G_R\, G_T\, N_{coh}}{(4\,\pi\, R^2)^2}$$

Acoustic transmitters and receivers differ in construction from EM antennas. The basic mode of translating pressure differences into the electrical domain is through piezoelectric crystals. The devices used in the experiments here will be discussed later.

An important consideration in both media is the concept of the far field. This describes the point at which the wave ceases to look spherical at a local point in space and appears to be planar. Clearly, an infinite plane wave containing infinite energy isn't physical, but it is convenient. This plane wave approximation greatly simplifies the mathematics required to calculate wave interactions and is generally an acceptable approximation if it stays within a local area and far enough away from the transmission source. The heuristic definition of the range to far field R_{ff} is as follows.

$$R_{ff} = \frac{2\,D^2}{\lambda}$$

This depends on the physical dimension of the antenna D, and the wavelength, λ, of the transmitting signal.

2.2 Advanced Radar Concepts

2.2.1 Direction Finding

One advanced capability of remote sensing that can be achieved with radar is that of direction finding. When plane wave impinges on a linear array of antennas, the phase difference between each antenna can be measured by the system.

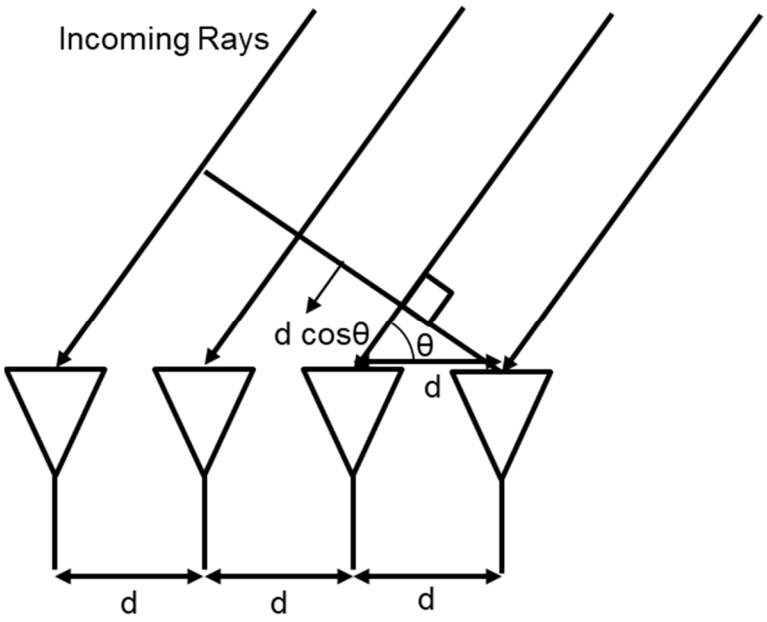

Figure 8: A plane wave impinging on a ULA

The most basic shape of a direction-finding array is that of a uniform linear array (ULA). This is constructed of identical receive antennas spaced at half the wavelength, d, apart from each other. The spacing requirement is a manifestation of the Shannon-Nyquist sampling theorem in the spatial domain. For a wave approaching from 0° and 180° to be adequately sampled, it must be done so twice per oscillation distance. The number of receive antennas also imposes a limit on how many simultaneous signals can be angularly resolved by the array. The limit is N-1 signals, where N is the number of ULA elements. This limit exists for commonly used direction-finding algorithms such as Minimum Variance Distortionless Response (MVDR) and MUltiple SIgnal Classification (MUSIC).

2.2.2 Synthetic Aperture Radar

Another form of remote sensing with radar that adds new capabilities to the system is synthetic aperture radar (SAR). As the name implies, this sensing method constructs a very large ULA using multiple collection points. This aperture enables very detailed processed return with image-like quality.

The enhanced resolution in the range dimension is enabled using LFMs. Since pulse compression will be employed, the range resolution as a function of the transmitted waveform's 3 dB bandwidth, *B,* is as follows:

$$\Delta x = \frac{c}{2\,\mathrm{B}}$$

SAR adds the ability to distinguish targets in the along-track direction. The length of the recorded track determines the along-track resolution. In a measurement the required length of the track, L_{req}, is the determined based on the desired along-track resolution, ΔL, that can be set preceding a data collection.

$$L_{req} = \frac{\lambda\, R}{2\,\Delta L}$$

Where R is the range of closest approach, and λ is the wavelength. Between each collection, a phase change is measured. If the object travels far enough between collections that this phase change increases beyond $\lambda/2$ the Doppler results become ambiguous. The 3 dB beam width of the transmitter antenna, β, determines the maximum movement distance, d_{max}, that avoids these Doppler ambiguities.

$$d_{max} = \frac{\lambda}{4\sin(\beta/4)}\ (meters)$$

This dictates how often the scene needs to be spectrally sampled along the track. Traditionally, these collections have been performed with airborne and spaceborne apparatus. A method of collection using a significantly smaller setup will be detailed later in the paper.

3 Equipment

3.1 Processing in MATLAB

All processing was done with the MATLAB programming language. This was done out of convenience since it comes standard on the School of Engineering computers and is the language

of choice for the KU Electrical Engineering curriculum. None of the programming used is exclusive to the MATLAB language and could be implemented other languages such as Python or C.

The direction finding and SAR processing were performed using scripts provided by my colleagues at the KU RSL lab. The MVDR script for direction finding was made by Christian Jones and the SAR Range-Doppler Algorithm (RDA) script was written by Daniel Herr. All the scripts written by me will be available in Appendix A which will include the data processing and the figures generated in this paper.

3.2 Test Hardware

3.2.1 Transducers

For all the experiments, the transmitting device was a transducer centered at 40 kHz. Normally, piezoelectric devices are very high Q resonators. As discussed in the theory section, radar applications benefit greatly from wide bandwidth signals. For the transducers to be able to transmit wide bandwidth signals the Q value must be spoiled. Details regarding transducer spoiling can be found in [1]. This spoiling procedure results in a transmission percent bandwidth much higher than a standard RF system. Standard RF antenna operate at about 10% bandwidth. The spoiled transducers used here can operate at 25% bandwidth (10 kHz at a 40 kHz). This allows for wideband testing without a complicated transmitter setup.

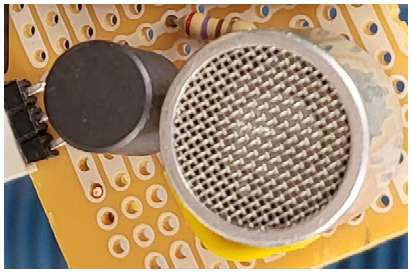

Figure 9: Spoiled transducer mounted on perfboard

As can be seen in Figure EQ1, the 16.2 mm diameter of the Kobitone 255-400ST16-ROX transducer does not easily permit for a half-wavelength (4 mm) spacing between devices. This means that beamforming on transmit is not available. Another feature of piezoelectric devices is that they follow reciprocity. Not only will an electrical signal excite an acoustic wave from the transducer, but an incoming acoustic wave will cause an electrical signal through the transducer. This can cause the transducer to self-modulate if there is an object directly in front of the device.

3.2.2 Microphones

The receive device used is a Knowles SPU0410HR5H-PB microphone. Instead of using a piezoelectric device, a MEMS microphone was used. These microphones have a wide bandwidth. They also have a high sensitivity due to their built-in amplifier but need a power supply. The most important feature is their size. With only a 3.76 mm x 2.95 mm footprint, they're perfect for creating a one or two dimensional array.

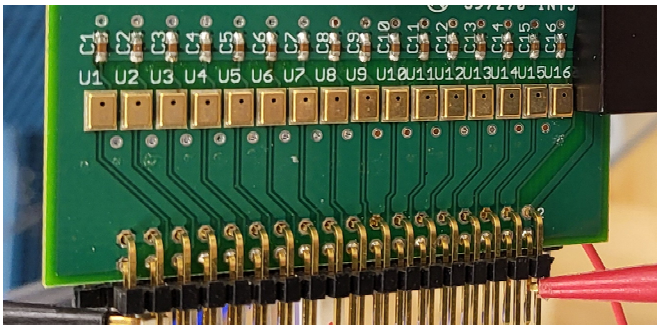

Figure 10: A 16 element ULA of microphones

These microphones have an extremely wide bandwidth of 100 Hz to 60 kHz and are omnidirectional. In addition to the intended receiver, there is also the unintended receiver of the cables connecting the microphones to the test equipment. In a noisy RF environment, such as a university, there are a multitude of communication signals that can couple into the cables. The most bothersome signal encountered during testing was an LTE uplink band around 700 MHz. This interference regularly caused the traces on the scope to clip and render the collection

useless. This issue was solved by introducing 300 MHz low pass filters on each of the signal lines. The frequency of the filters was chosen because the parts were on hand and rejected this interference signal.

3.3 Loopback Methodology

Matched filtering is a common radar technique used in conjunction with pulse compression. This matched filter is often formed from loopback data. In a RF system the waveform is propagated through the TX chain and then directly connected to the RX chain through an attenuator to achieve loopback measurements. This characterizes the distortions from devices such as amplifiers and mixers in either chain. The antennas and array distortions are not considered in this setup. In a sodar system, the distortions coming from the transmitting and receiving devices are considered.

The sodar loopback setup consists of a short range over the air transmission instead of directly connecting the TX and RX chains. The distance must be long enough to avoid the TX transducer from self-modulating due to acoustic reflections from the RX device. This effect is evident by a large AM present on the Rx signal. In these experiments this distance was empirically measured to be approximately 1 dm.

In an RF loopback measurement, there is effectively zero delay between transmission and reception. With the sodar setup this is non-zero. This results in a shifted peak when correlating the loopback waveforms with the theoretical waveforms. This can be corrected by imposing a phase offset compensating for the phase acquired during transmission.

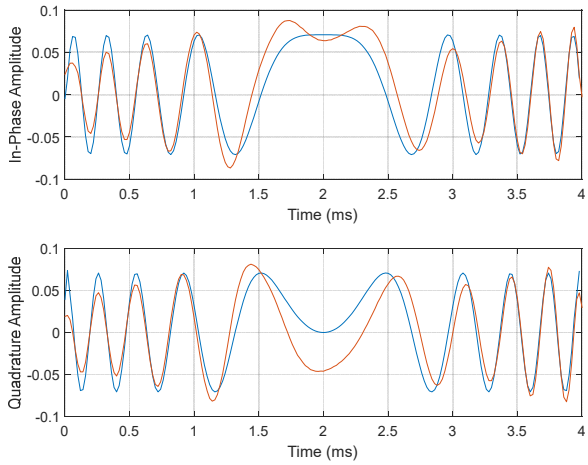

Figure 11: Time-domain in-phase and quadrature amplitudes for ideal (blue) and loopback (orange) LFM waveform.

From testing, the transducer imposed a 1 dB mismatch loss compared to the theoretical signal for an LFM. This result will be used to form the matched filter for the experiments later.

3.4 Objects

3.4.1 Trihedral

The passive object used for detection is a standard RF trihedral. The brass material that allows for great EM reflection also works well for acoustic reflections. The wave physics that enable a trihedral to appear as a point target for EM also work for acoustic.

Figure 12: The 3 in and 6 in trihedrals used for experiments

The 3 in trihedral was the SAGE SAJ-032-S1 and the 6 in trihedral was the SAGE SAJ-060-S1. These were acquired for millimeter wave experiments and work well for acoustic waves. The 40 kHz acoustic wave is also in the millimeter wave regime, and the smoothness provides a continuous reflective surface. A comparable return was measured from a baking sheet affixed to a painter's easel. However, these were available for testing and are much easier to move.

3.4.2 Active Transmitters

In the direction finding experiment the premise is that the system is passive. This means that the objects were active transmitters that were emitting certain signals. This setup also enables experiments that are closer to that of a simulation. Instead of the objects reflecting a signal from a colocated transmitter and receiver, they can instead transmit a signal directly.

3.5 Waveform Generators

3.5.1 Agilent Waveform Generator

Figure 13: The Agilent waveform generator

The waveform generator used for the basic radar experiments was the Agilient 33250A. The maximum output frequency is 80 MHz, which is more than enough for a 40 kHz tone. The burst mode was used with a 40 kHz sine wave to produce a gated sinusoid pulse. For continuous wave (CW) operation, the generator produced a constant 40 kHz tone. The Sync output provided a trigger source for the scope. The output was split so that it was viewed by the scope while also

being transmitted. This particular model has the license for the arbitrary waveform generator. With the assistance of a laptop, a waveform less than 64kB can be loaded.

3.5.2 Tektronix Arbitrary Waveform Generator

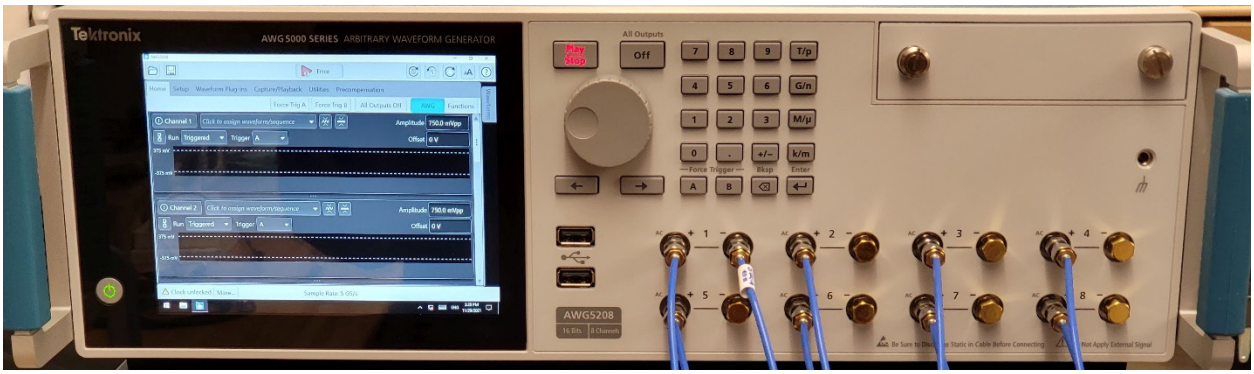

Figure 14: The Tektronix waveform generator

The waveform generator used for the direction finding and SAR experiments was the Tektronix AWG5208. For the direction finding experiment the arbitrary capability was needed for transmission of the orthogonal frequency division multiplexed (OFDM) communications signal and the random frequency modulation (RFM) interference. Although this was used to generate an LFM for the SAR experiment, there exists many less expensive waveform generators that will produce an LFM. This waveform generator has the convenient feature of being able to take in MATLAB files directly and transmit. In other systems, the data must first be converted into another format before being used. This allowed for quick iterations on experiments. The arbitrary nature of the transmit waveforms also allows for a focus on waveform design in experiments. This advantage will not be discussed in this paper.

3.6 Oscilloscopes

3.6.1 Keysight Scope

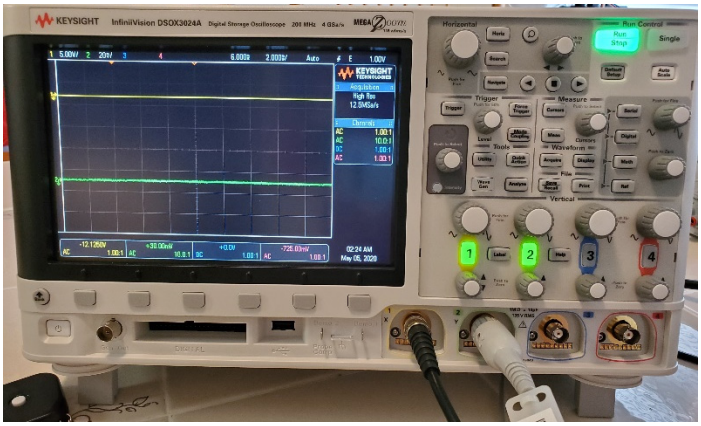

Figure 15: The Keysight oscilloscope

The scope used for the basic radar experiments was the Keysight DSOX3024A Digital Storage Oscilloscope (DSO). This four-channel scope has an analog bandwidth of 200 MHz and a maximum sample rate of 4 GS/s. The sample rate is coupled to the horizontal scale. At the time scales used in these experiments the scope varied between 12.5 to 100 MS/s. The analog bandwidth was significantly higher than the 40 kHz required by the ultrasonic setup. The sample rate was also more than the needed 80 kHz to sufficiently sample the signals. The Keysight scope came with all the analysis tools needed for the basic radar experiments. Markers measured the delay to be used in range calculations, and the built-in FFT provided spectral domain data. Coherent integration in slow time was also available up to 64 collections. A built-in high-resolution mode performs 16x fast-time coherent averaging yielding a 12-bit vertical resolution while suppressing noise.

3.6.2 Tektronix Oscilloscope

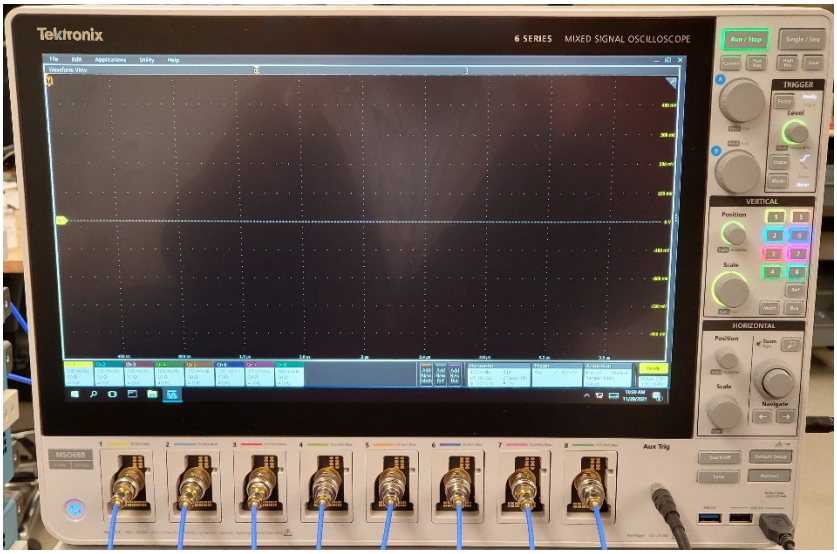

Figure 16: The Tektronix Oscilloscope

The oscilloscope used for the direction finding and SAR experiments was the Tektronix MSO68B. The eight available channels allowed for more precise direction finding. For the SAR experiment, the more useful feature was the improved “High Res” mode compared to the Keysight scope. Since the channels on the MSO68B always sample at 12.5 GS/s, the samples beyond what are requested are used for fast time coherent integration. This means that a signal with a requested 5 MS/s output will benefit from a processing gain of 34 dB. The ability to decouple the sampling rate from the record length was also useful. This allowed similar processing across collections of different record lengths. Traces were also able to be saved directly as MATLAB data files. This expedited information unpacking during processing and contributed to faster iterations. Although a very expensive scope was used for these experiments, it wasn’t necessary. The 4 GHz available analog bandwidth, which is significant portion of the cost, was not utilized. The High Res mode was a significant time-saver since it performed the coherent integration in fast time, but this could also have been achieved with multiple collections

in a slow time fashion. For ultrasonic systems, the analog bandwidth requirements are very low, and this is the main driver of high-price oscilloscopes.

4 Experiments

4.1 Basic Radar Concepts

4.1.1 Setup

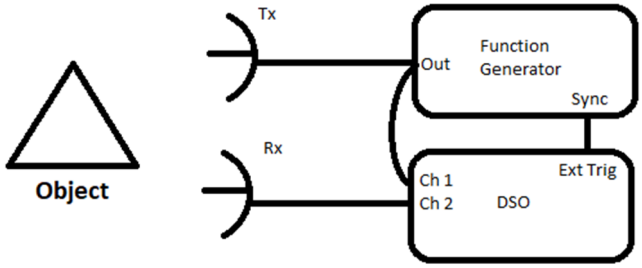

Figure 17: Block Diagram of the sodar setup used in the basic radar experiments

The sodar setup consisted of the parts shown in Figure 17. The waveforms used for testing were 40 kHz sinusoids generated by the 33250A Agilent Function Generator. The length of the pulsed operation was varied by changing the number of cycles in the sinusoid pulse. For continuous wave (CW) operation, the 40 kHz sine wave was run continuously.

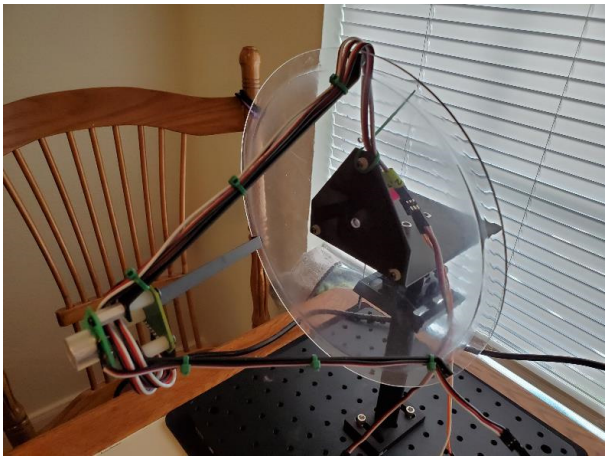

Figure 18: Physical transceiver setup

The transmitter and receiver were the transducer and microphone mentioned in the equipment section. The transducer was fed a 1 Vpp signal directly from the waveform generator. The

microphone located behind the transducer board receives the returned signal after it bounces off the parabolic reflector. The distance between the microphone and reflector is 14 cm. This distance will be important for range calculations. From one meter away the returned signal strength was approximately 10 mV. The next step in the chain is the oscilloscope. This was the Keysight DSOX3024A.

4.1.2 Range and Range Resolution

The two objects used consisted of a 3 in trihedral at .61 m from the transmitter and a 6 in trihedral at 1.0 m. The smaller one will be referred to as object 1 and the larger one will be referred to as object 2.

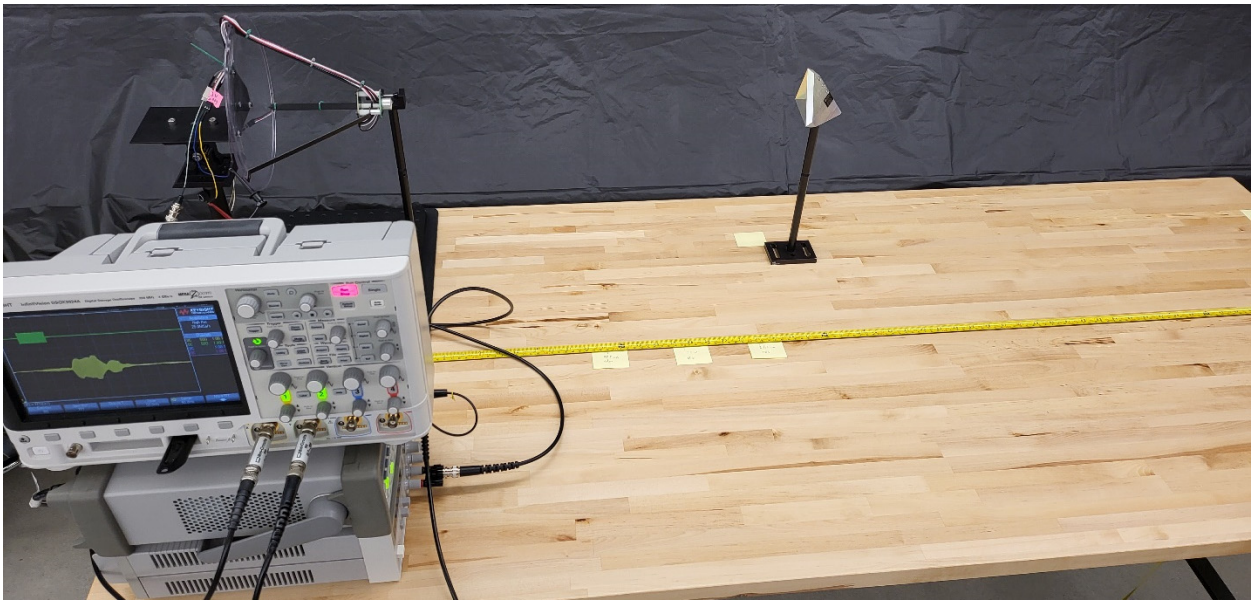

Figure 19: Range setup using Object 1

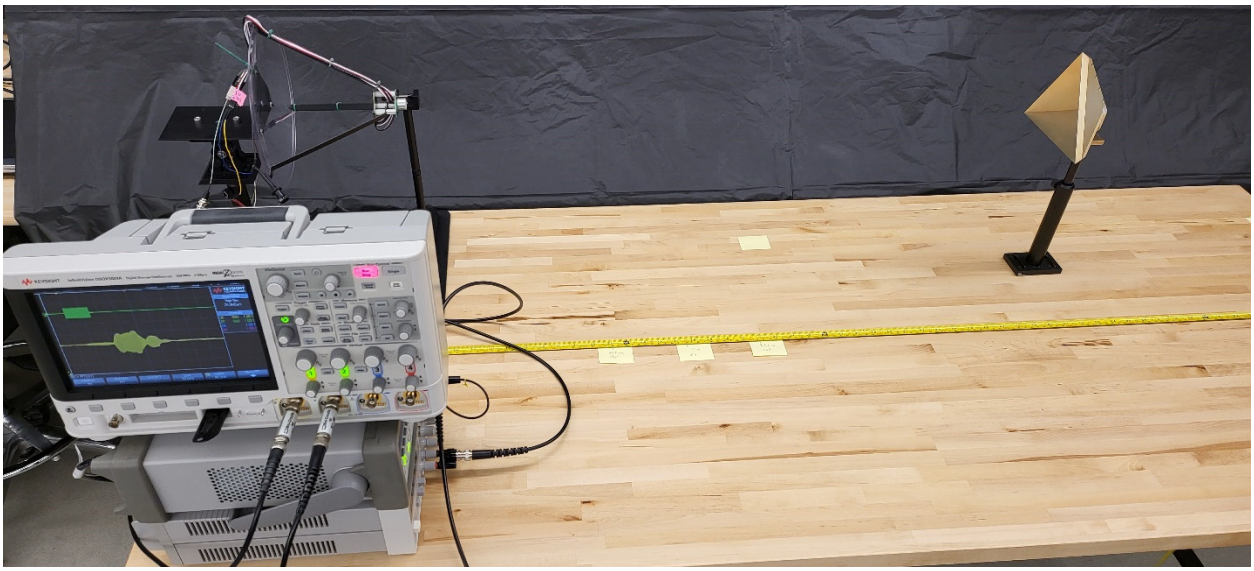

Figure 20: Range setup using Object 2

This experiment will use the equations highlighted in section 2.1.1. There are a few modifications to the equations due to the physical setup of the transceiver and the acoustic wave being used. Even though the transmitter and receiver are attached to each other, the returned signal travels farther than the transmitted signal since it must bounce off the parabolic reflector. This distance between the microphone and reflector is 14 cm. Twice this distance, due to the bounce, must be added to the right side of the equation to properly calculate the distance from the transmitter to the object. Another change is that instead of using the speed of light one must use the speed of sound c_s, which is 340 m/s. This speed was measured at the same elevation that the experiments were performed. Taking these changes into account the range formula becomes:

$$R = \frac{T * c_s - 0.28}{2} \quad \text{(Eq. 1)}$$

From a setup using object 1 the following transmitted and received signal was captured:

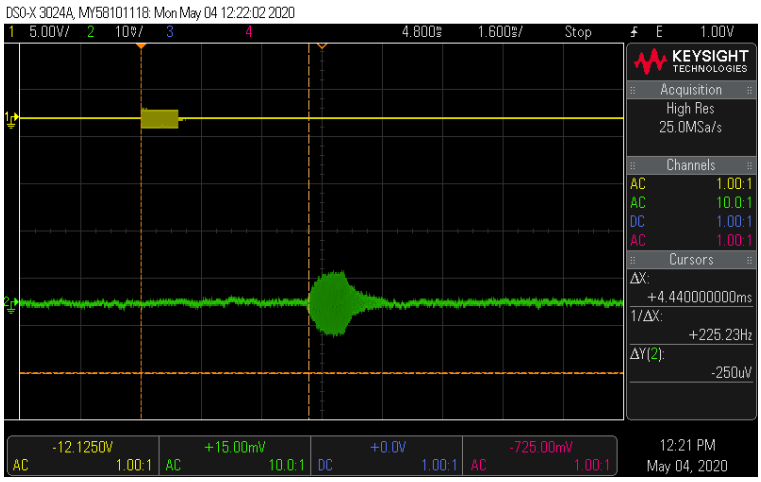

Figure 21: A generated (yellow) and received (green) signal from object 1

The transmitted signal is a gated sinusoid. The received signal differs in shape and length from the transmitted signal. The bulk of the response is the same length, but there seems to be a tail extending past the main return. The received signal is dissimilar to the generated signal due to the distortion imposed by the transducer. This distortion can be compensated for by predistortion of the waveform if desired. However, the important part is the start of the return which is used to measure range by plugging the delay into Eq. 1.

$$R = \frac{0.00444 * 340 - 0.28}{2}$$

$$R = .61\ m$$

This measurement agrees with the distance that object 1 was placed at. Using the setup containing object 2, the following data was collected.

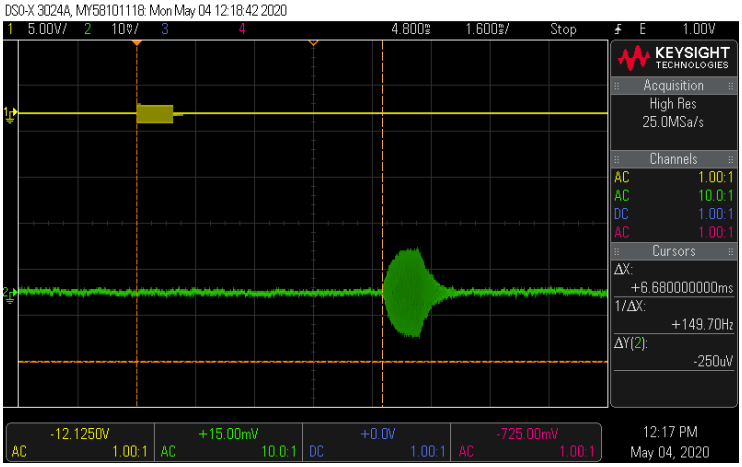

Figure 22: A generated (yellow) and received (green) signal from object 2

As expected, the farther object has a longer delay between transmit and receive. This return is also a larger magnitude since object 2 is physically larger than object 1. This delay, when entered into Eq. 1 gives the following result:

$$R = \frac{0.00668 * 340 - 0.28}{2}$$

$$R = 1.0\ m$$

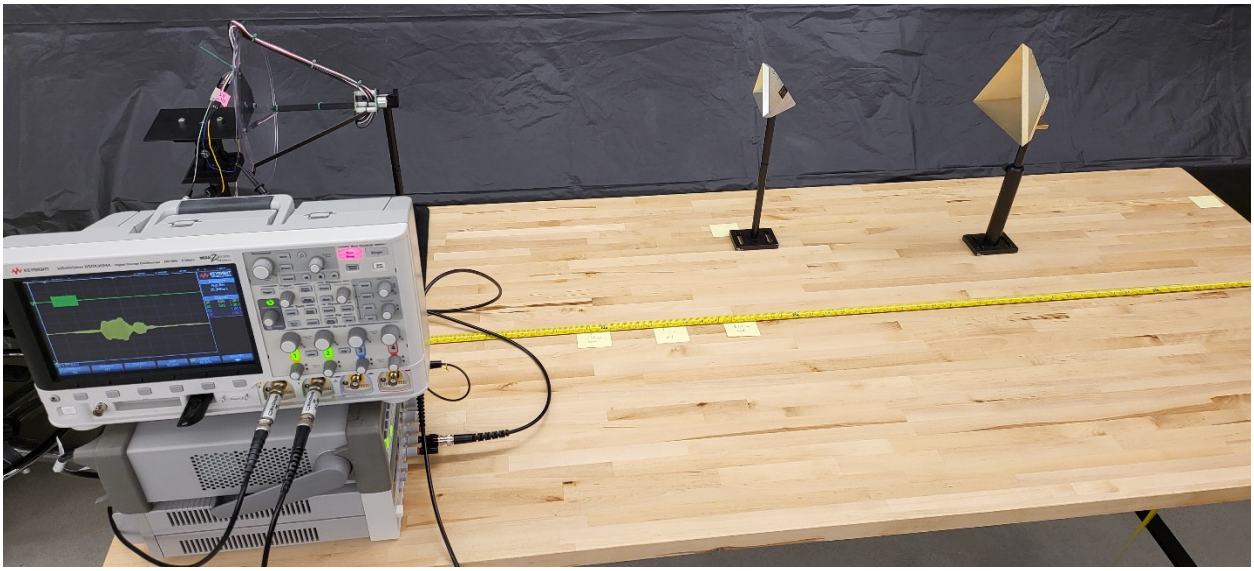

Figure 23: Range Resolution setup using Object 1 and 2

Having more than one object in the scene adds complexity to the measurement and involves the topic of range resolution. At a certain pulse length, two separate returns will become combined if they get closer than a certain range. It can be described mathematically as shown in the theory section as:

$$\Delta R = \frac{c\,\tau}{2}$$

Since the pulse length τ can be more accurately controlled and measured in this setup, the equation is rearranged for a static separation ΔR. This can be described as how long of a pulse length can be transmitted before two close returns become muddled.

$$\tau = \frac{2\,\Delta R}{c} \qquad \text{(Eq. 2)}$$

Using the measured ranges from the first set of experiment it can be determined that the ΔR is 39 cm. Plugging that value into Eq. 2 gives:

$$\tau = \frac{2 * .39}{340}$$

$$\tau = 2.29\,ms$$

What this means is that once the pulse length becomes greater than 2.29 ms the two objects will be indistinguishable.

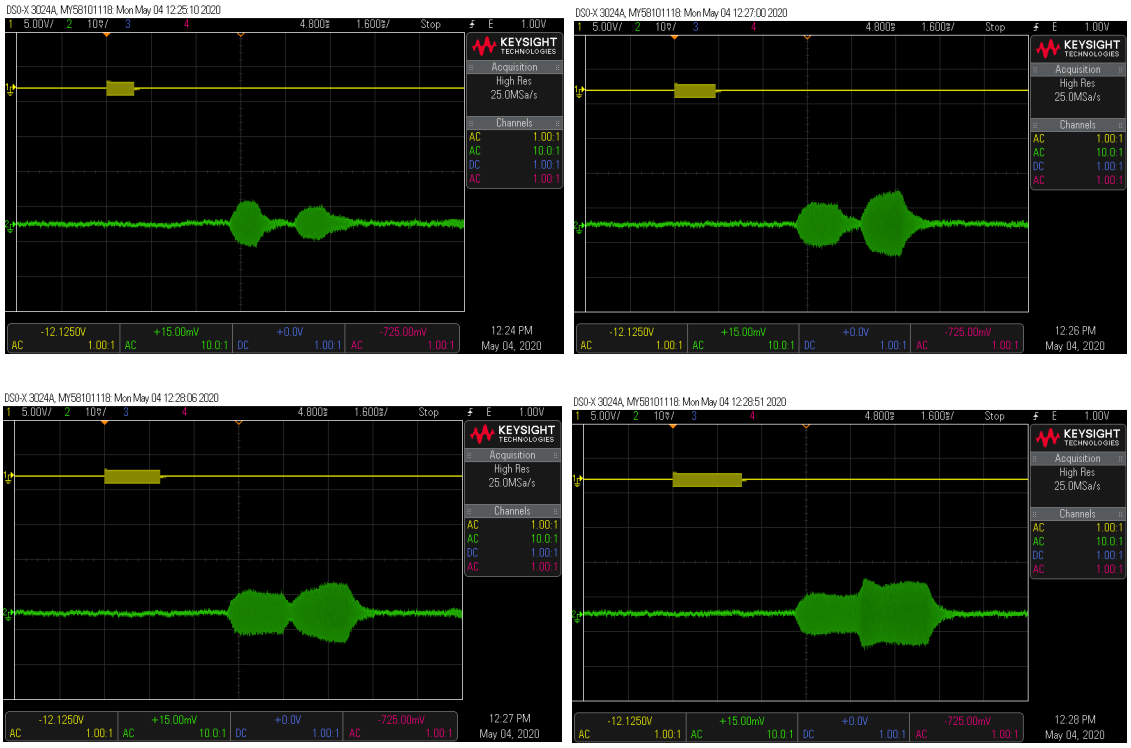

Figure 24: Tx and Rx with pulse durations of 1, 1.5, 2, and 2.5 ms

As can be seen from Figure 24, when the pulse duration becomes longer than 2.29 ms the two object responses become merged.

4.1.3 Doppler

For the Doppler experiment, the waveform generator was set to a CW operation at 40 kHz. In order to generate a Doppler effect a swinging apparatus was constructed from available optical breadboard components as shown in Figure 25.

Figure 25: Swinging object apparatus

By taking advantage of the Doppler effect, the radial velocity of an object can be measured. The Doppler offset can be described mathematically as shown in the theory section as:

$$f_D = \frac{2\,v}{\lambda}$$

Where v is the radial velocity and λ is the wavelength of the transmitted signal. At 40 kHz the wavelength of the sound wave is .85 cm. Since the scope will be measuring the frequency offset, the equation can be rearranged to find the radial velocity.

$$v = \frac{f_D\,\lambda}{2} \qquad \text{(Eq. 3)}$$

Using the sodar setup the following measurements were taking on a moving object 1.

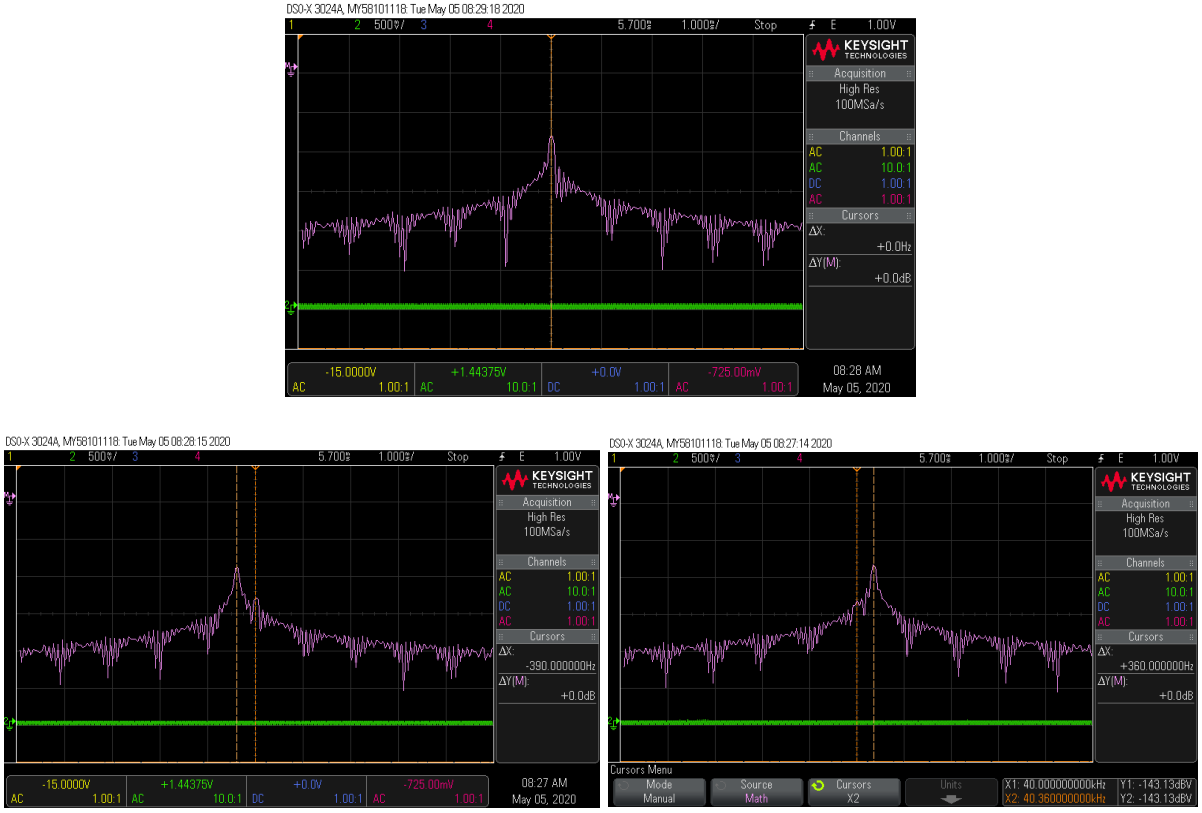

Figure 26: FFT of Rx signal with no movement, backwards movement, and forwards movement

Frequency offsets of -390 Hz and 360 Hz were recorded for backwards and forwad movement respectivily. These results when entered into Eq 3 Give results of -1.66 m/s and 1.52 m/s. With a rod length of approximatly 17 cm, the maximum speed at the bottom of the swing is 2.2 m/s. Both of these values are below that maximum, which passes the sanity check. The loss of velocity is most likely due to the friction in the mount.

4.1.4 Pulse Compression

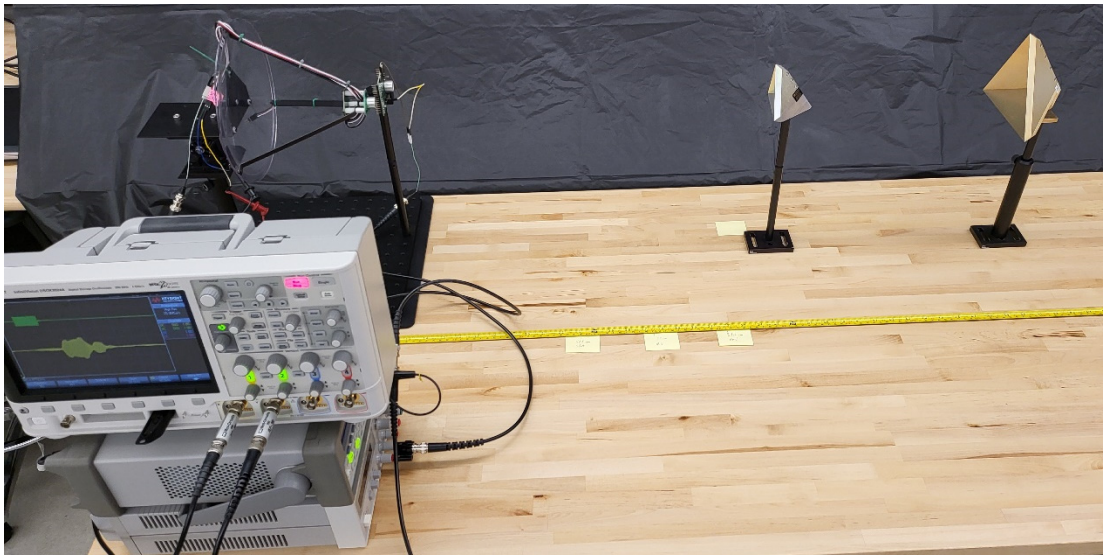

Figure 27: Pulse Compression setup using Object 1 and Object 2

The object placement for this experiment was identical to the range resolution test, which the exception of the transducer. The transducer built into the parabolic reflector is not spoiled, so a spoiled one was placed in front of it, as can be seen in Figure 27.

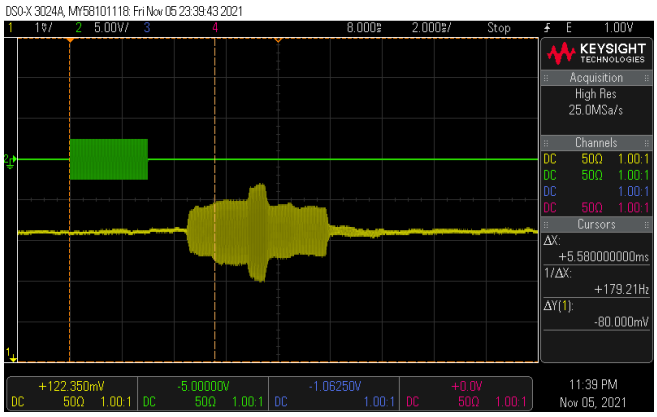

Figure 28: The transmitted signal (green), and the received return (yellow) from a 3 ms pulse

As can be seen in Figure 28, the pulse duration does not enable the two objects to be separately resolved. By adding bandwidth in the form of a chirped sinusoid, as discussed in the theory section, the two objects can be resolved after processing.

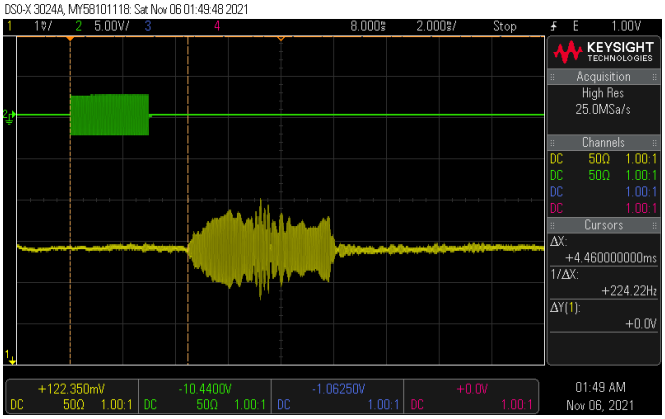

Figure 29: The transmitted signal (green), and the received return (yellow) from a 3 ms chirped pulse

The transmitted waveform was a 6.5 kHz LFM chirp centered at 40 kHz, which results in a range resolution of 2.6 cm. In the time domain the response seems to still be a jumbled mess. However, after matched filter processing, the two objects can be resolved as shown in Figure 30.

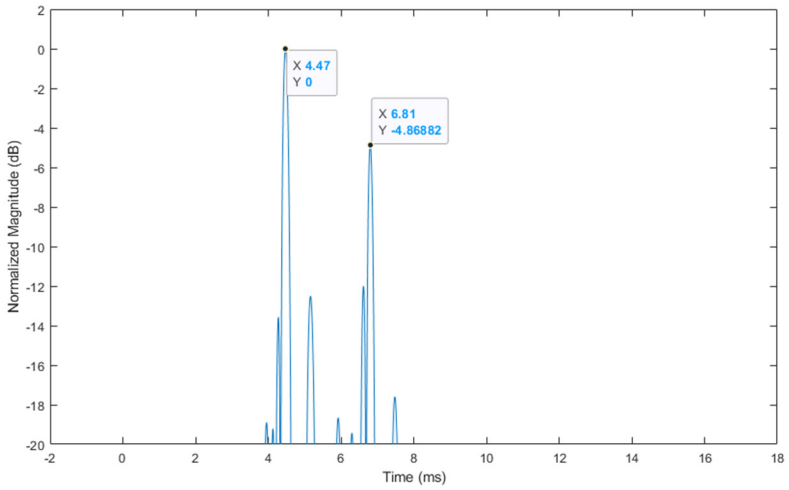

Figure 30: The received data after processing in MATLAB showing two clear responses

4.1.5 Coherent Averaging

Using the object 2 setup, the function generator was set up to repeat the same burst. This allowed for the different pulse returns to be combined in slow time to demonstrate the benefit of coherent averaging. As previously mentioned, the noise decoheres and the signal coheres. As the

different samples accumulate more of the returned signal becomes clear as the noise is suppressed.

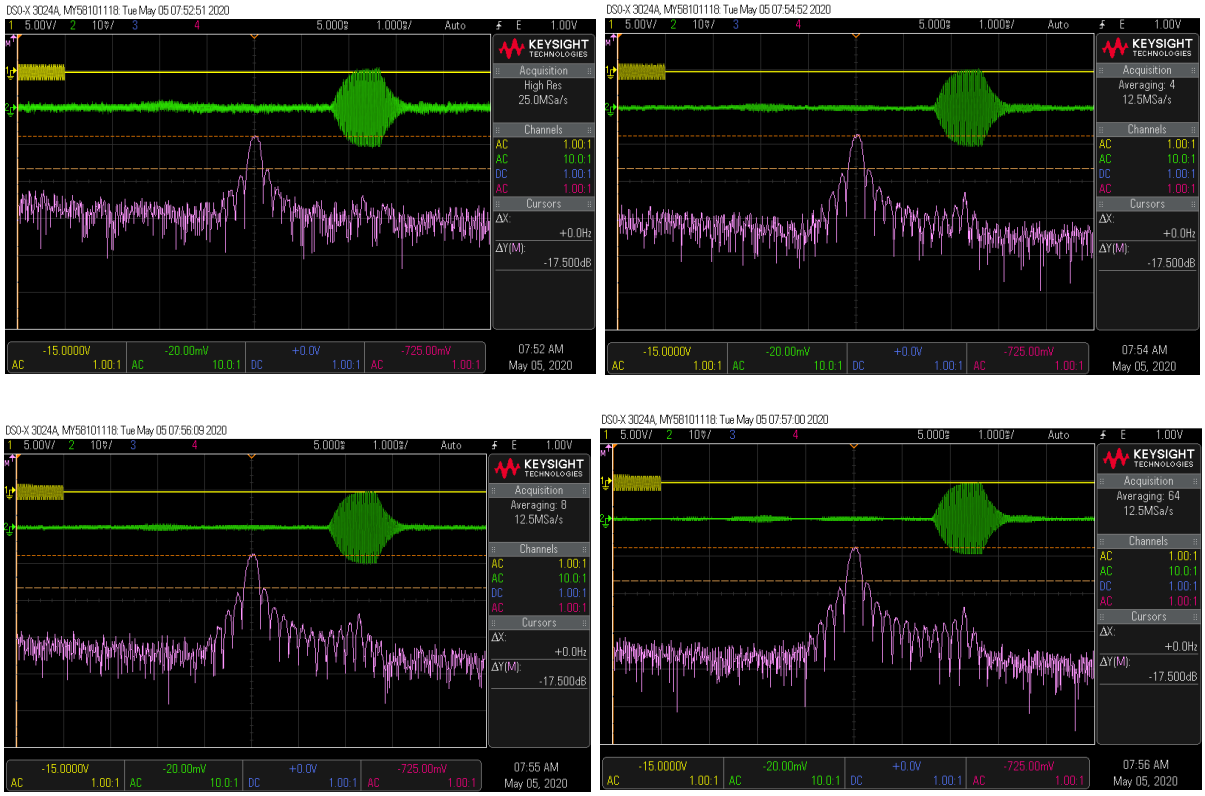

Figure 31: Tx, Rx, and FFT of the RX (pink) at 1, 4, 8, and 64 integrations

This shows how a second resonance point of the transducer previously burried in the noise becomes visible with the use of coherent integration.

4.1.6 Windowing

Using the object 1 setup and having the function generator in CW mode windowing functions can be explored. The Keysight scope come with a few of the most popular windows. As the windows become more complex, the sidelobes are further repressed.

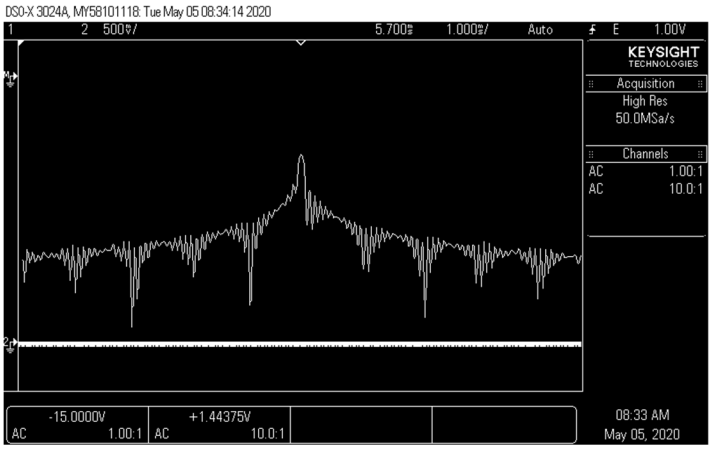

Figure 32: The rectangular windowing function applied to FFT of the return

This is the standard windowing function and serves as a baseline to the others are.

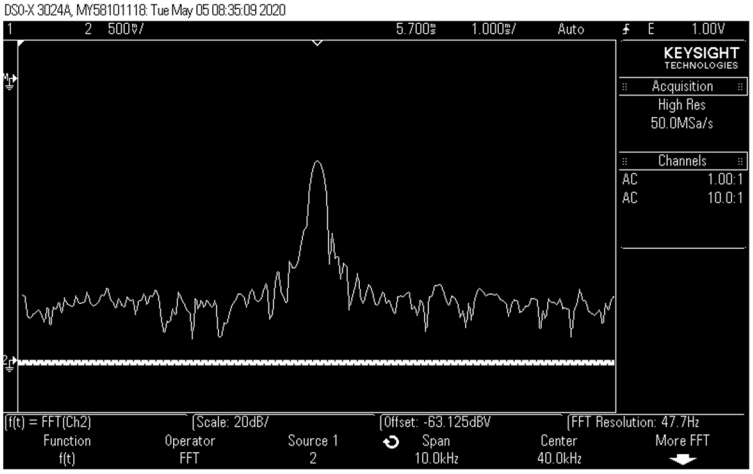

Figure 33: The Hanning windowing function applied to FFT of the return

The Hanning window drives down the sidelobes much farther than the rectagular window.

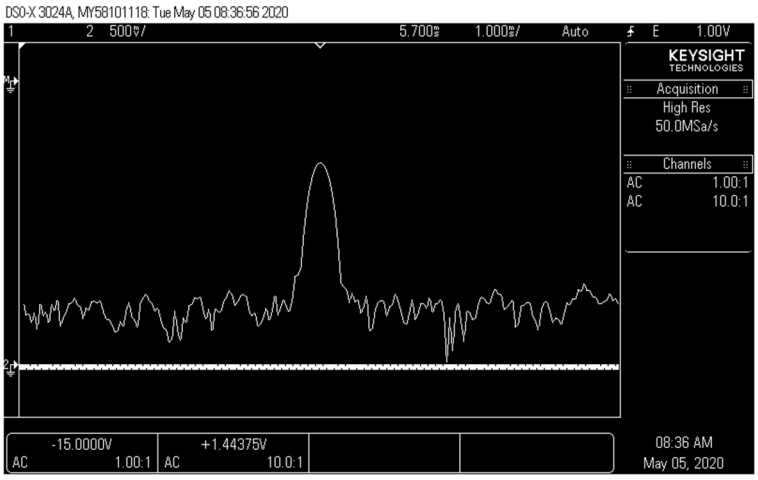

Figure 34: The Blackman-Harris windowing function applied to FFT of the return

The Blackman-Harris window offers the best sidelobe suppression, but at the cost of a widened main lobe.

4.2 Advanced Radar Concepts

For the advanced radar concepts section, the MSO and AWG will be utilized. The arbitrary waveforms were needed for the direction-finding portion, and the fast time coherent averaging from the MSO provided a massive signal to noise ratio improvement. Each experiment has a distinct setup instead of using the same general setup for both.

4.2.1 Direction Finding

The direction-finding setup used three spoiled transducers as transmitters. The receiver was 8 channels of a 16-channel array. The transmitters were arranged relative to the receiver as shown in Figure 35.

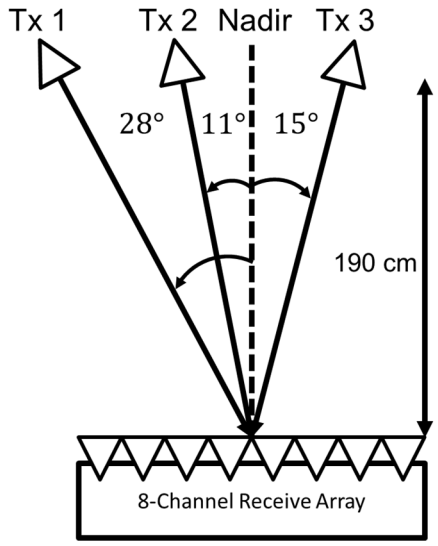

Figure 35: Setup of direction-finding experiment

Transmitter 1 transmitted a frequency modulated continuous wave (FMCW) signal, transmitter 2 transmitted an OFDM signal, and transmitter 3 transmitted random frequency modulated noise. The angles of arrival were calculated using a tape measurer and trigonometry. Each transmitter was place in a plane parallel to the receive array to enable these calculations.

Figure 36: Mounted transmitters and receiver

The transmitters and receivers were mounted using optical breadboard equipment. The receive array was connected to the oscilloscope using a jumper connected to a BNC connecter via a 50

Ohm transmission line. The transmitters were directly connected to the AWG. Each channel on the AWG was generating its signal at 750 mV peak to peak. This was a significantly lower amplitude than in the basic radar experiments. This low signal power was compensated for by using the fast time coherent averaging effect of the oscilloscope.

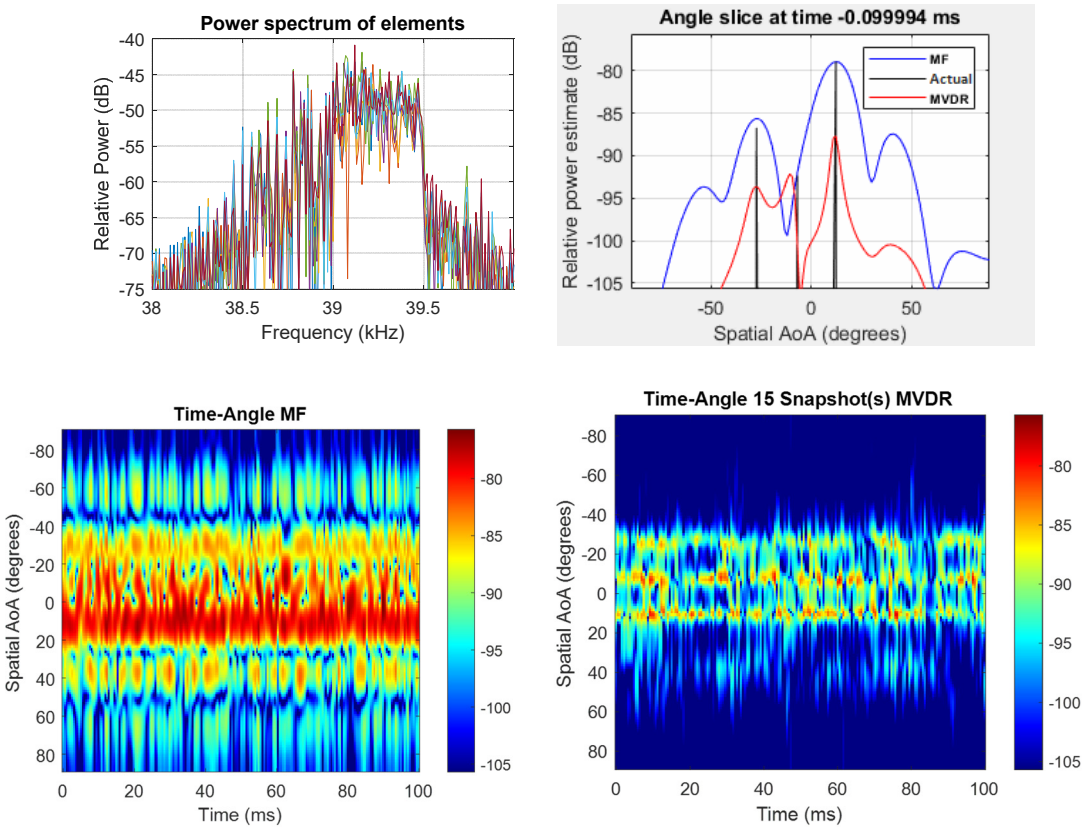

Figure 37: Power spectrum of signals (a), frequency slice of MF and MVDR results (b), spectrogram of MF processing (c), spectrogram of MVDR processing (d)

The combined received signal is shown in 37a. The most basic form of direction finding is using a matched filter (MF) method. This result is shown in Figure 37c. An adaptive form of direction finding, MVDR, is a considerable improvement, and is shown in Figure 37d. There are other direction-finding methods that demonstrate an improved signal isolation compared to MVDR

that have been experimentally demonstrated using this same setup [2]. Those methods will not be discussed in this thesis.

4.2.2 Ultrasonic SAR

In a standard synthetic aperture configuration, the scene remains static while the transmitter & receiver move linearly in the cross-track dimension. Alternatively, an equivalent phase history can be collected by moving the scene in the cross-track dimension and allowing the collection apparatus to remain static. This alternate test configuration can be shown to be equivalent using the concept of reciprocity. The motivation for this alternate view is that moving a simple object can be much simpler than moving the more complicated transmitter & receiver apparatus. A general scheme is shown in Figure 38.

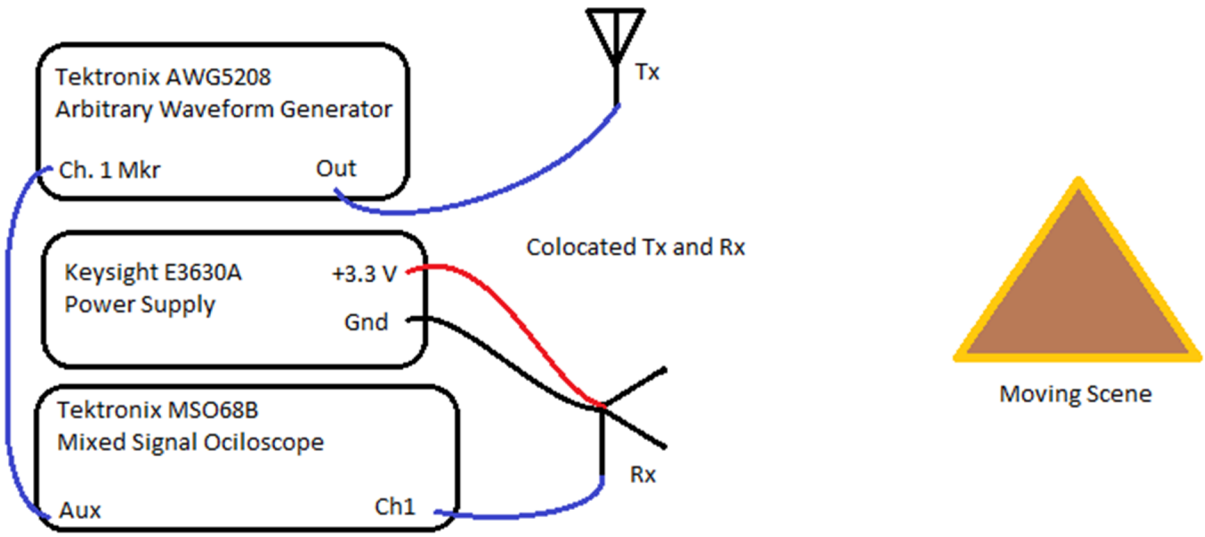

Figure 38: Experimental setup for SAR

The transmitter/receiver apparatus (Tx/Rx) is a colocated transducer and microphone, that are on separate boards, but clamped together on optical breadboard equipment. This is shown in Figure 39. The transmitter bandwidth is centered at 40 kHz and is 8.575 kHz wide. The microphone's

bandwidth is much wider than the transmitter's bandwidth. Using pulse compression, this results in a range resolution of 2 cm.

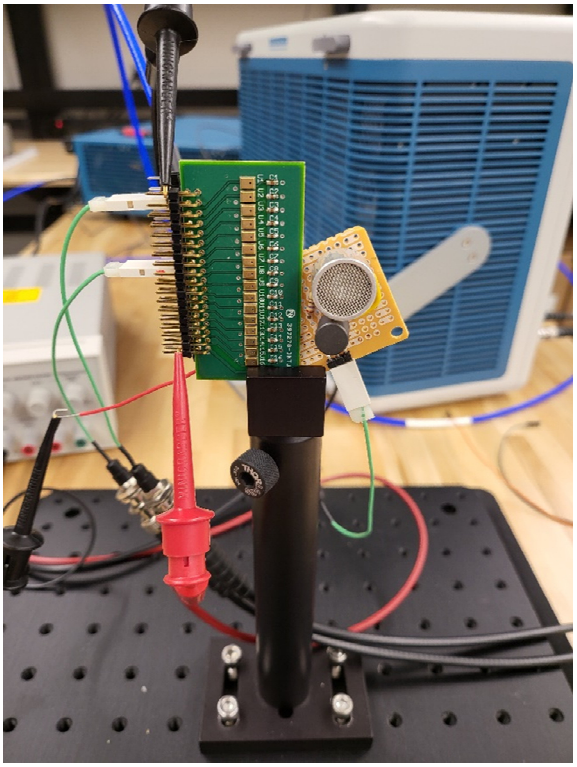

Figure 39: Tx/Rx configuration

The parameters used in this experiment were chosen using the equations outlined in the theory section and physical limitations of the test hardware. The transducer used is spoiled to have a bandwidth of 10 kHz. Inserting this value into the range resolution equation, along with the speed of sound, results in 1.72 cm being the finest range resolution possible with our available bandwidth. The bandwidth used was decided to be 8.575 kHz to obtain a nice round number of 2 cm for the range resolution.

In order to obtain square pixels in the SAR map, this required an along-track resolution of 2 cm. Inserting this into the required track length equation, along with the range of closest approach, 100 cm, and wavelength yielded a required track length of at least 21.44 cm

In order to prevent Doppler ambiguities, one must consider the maximum distance the scene can move between captures. Using the maximum movement distance equation, and the beam width of the transducer, 35°, the maximum movement between captures is found to be 7.1 mm. The actual movement distance was chosen to be 7 mm based on the limitations of the distance measurement and scene movement hardware.

Having the step size and the minimum length determined, simple arithmetic was used to find the number of steps that fit in the track minimum length of 21.44 cm. The result was rounded up to 31, because an integer number of steps was required. This resulted in a track length of 21.7 cm. The implementation of the moving scene is shown in Figure 40.

Figure 40: Implementation of moving scene

The 6 in trihedral was chosen to give a point-like response on the resulting SAR map. The trihedral rested on a sheet of acoustic absorber that allowed for the scene to be easily moved across the table and dampened the reflection of the table's edge.

A series of measurements representing a SAR phase history were collected. The phase history consisted of 31 collections of a trihedral that was moved in the along track direction across the ultrasonic transducers main beam. Note the invocation of the theory of reciprocity to allow for a

moving target instead of a moving SODAR. The phase history was then processed using the Range-Doppler algorithm described in [3]. The pulse compressed phase history is shown in Figure 41 and the resulting SAR map for the case of the LFM waveform is shown in Figure 43.

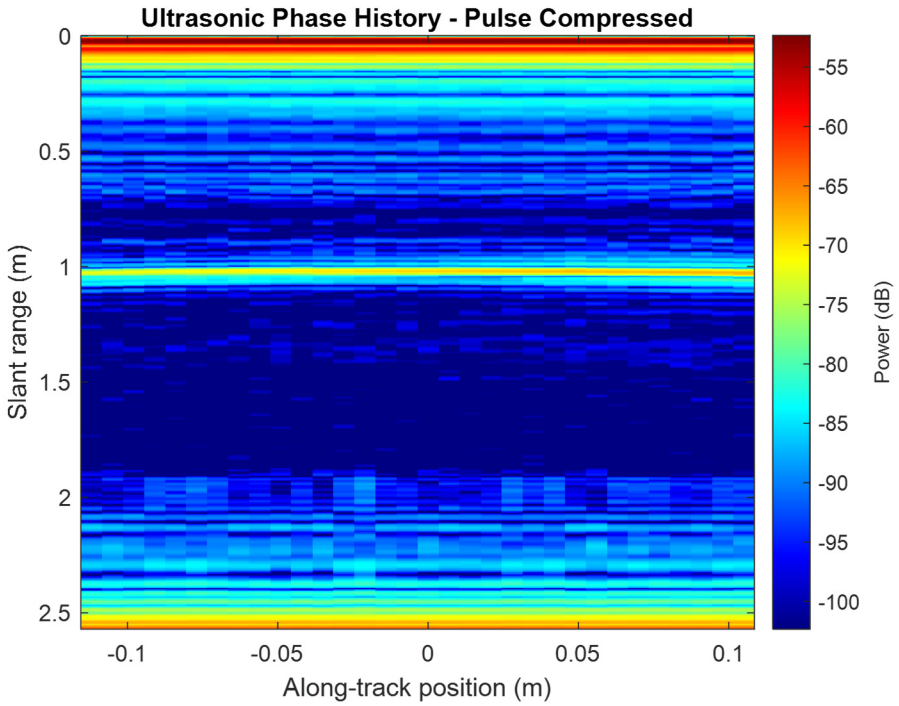

Figure 41: Pulse compressed phase history of the single object SAR collection

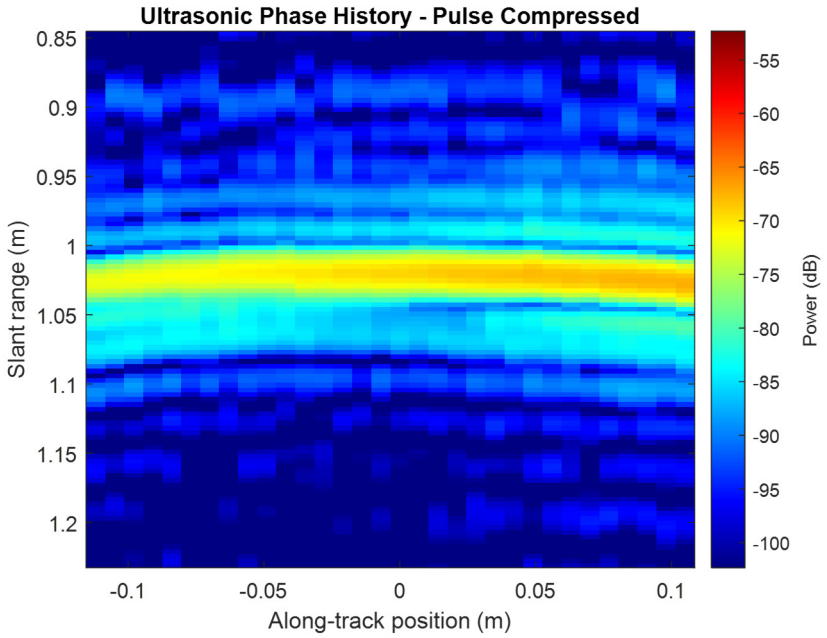

Figure 42: Pulse compressed phase history of the single object SAR collection with zoomed-in section

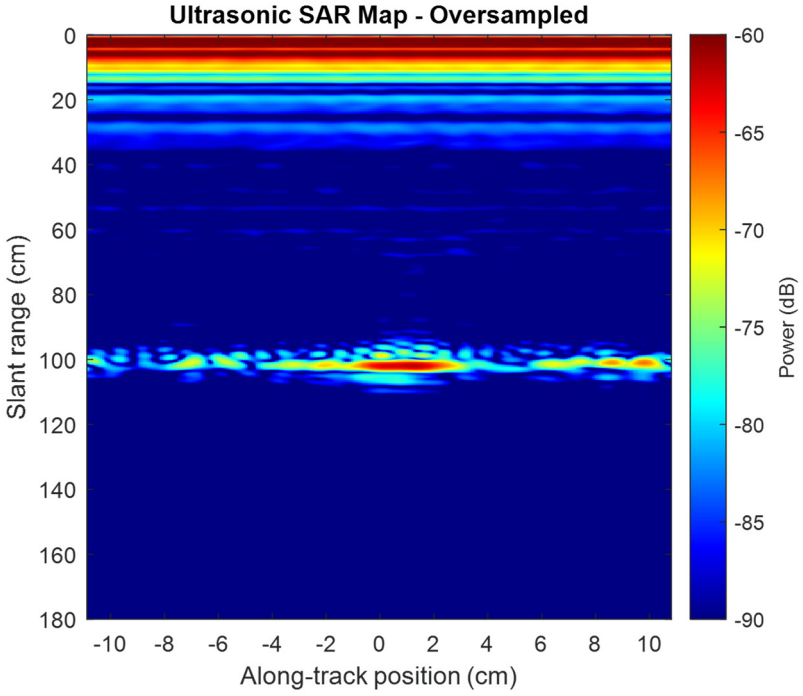

Figure 43: SAR map generated from LFM illuminated scene

Inspection of Figure 43 shows that the trihedral has been successfully resolved at a distance of 100 cm using the testbed. Also apparent in the SAR map is the direct path component from ultrasonic transducer; ranges 0 to ~40 cm.

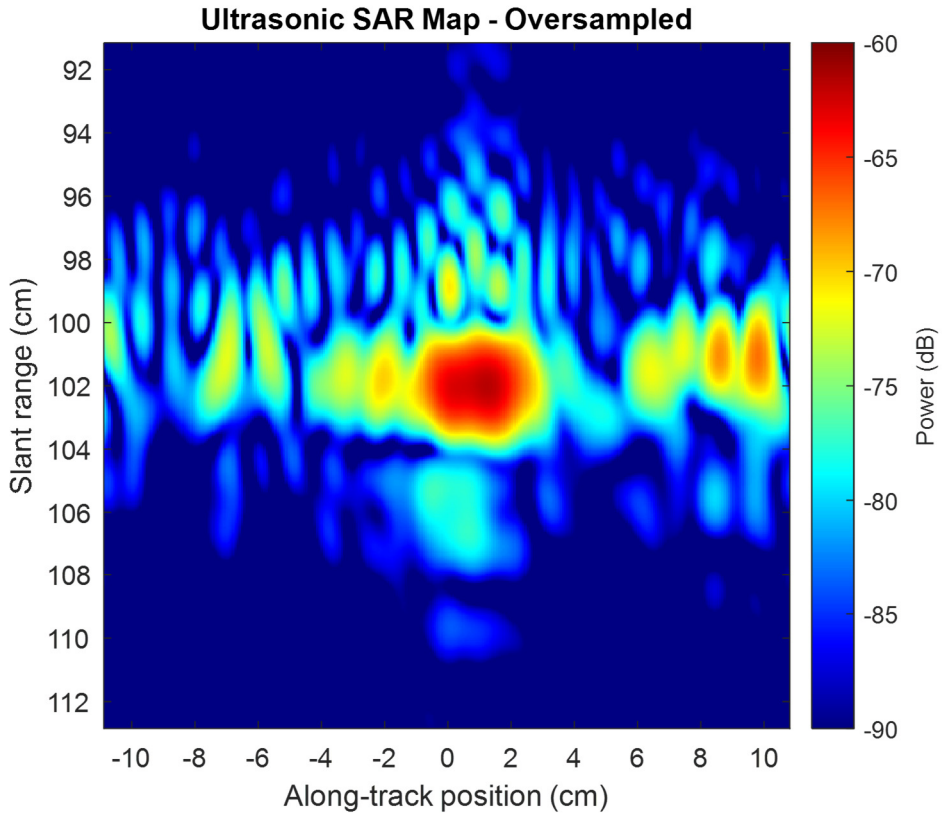

Figure 44: Zoomed in SAR map generated from LFM illuminated scene

Figure 44 shows the result of the RDA on the collected phase histories. The result has been oversampled to better show features. This result shows a resolved point object straddling the two central azimuth bins. The large streak across azimuth at 1 m range bin is a reflection from the table indicating that the acoustic absorber was not absorbent enough. The effects are non-uniform in azimuth because the absorber moves along with the trihedral providing a reflection that is not static in azimuth. In range, the object appears in the 100 – 102 cm range bin, meaning the object was slightly farther than the intended 100 cm. Although the scene only had one object,

there appears to be a response at an along-track position of 8 - 10 cm, this is most likely an azimuth sidelobe spreading across multiple azimuth bins.

After this successful demonstration a more complicated rig was constructed by Daniel Herr to perform SAR collections. This rig consists of a stepper motor moving a gantry along a one-meter long rail. A movable rig means that the transmitter and receiver setup shifts between collections, which resembles a traditional SAR collection method. Since the rig can repeatedly make fine movements, longer collection tracks and a finer azimuth resolution are possible. The rig is shown in Figure 45.

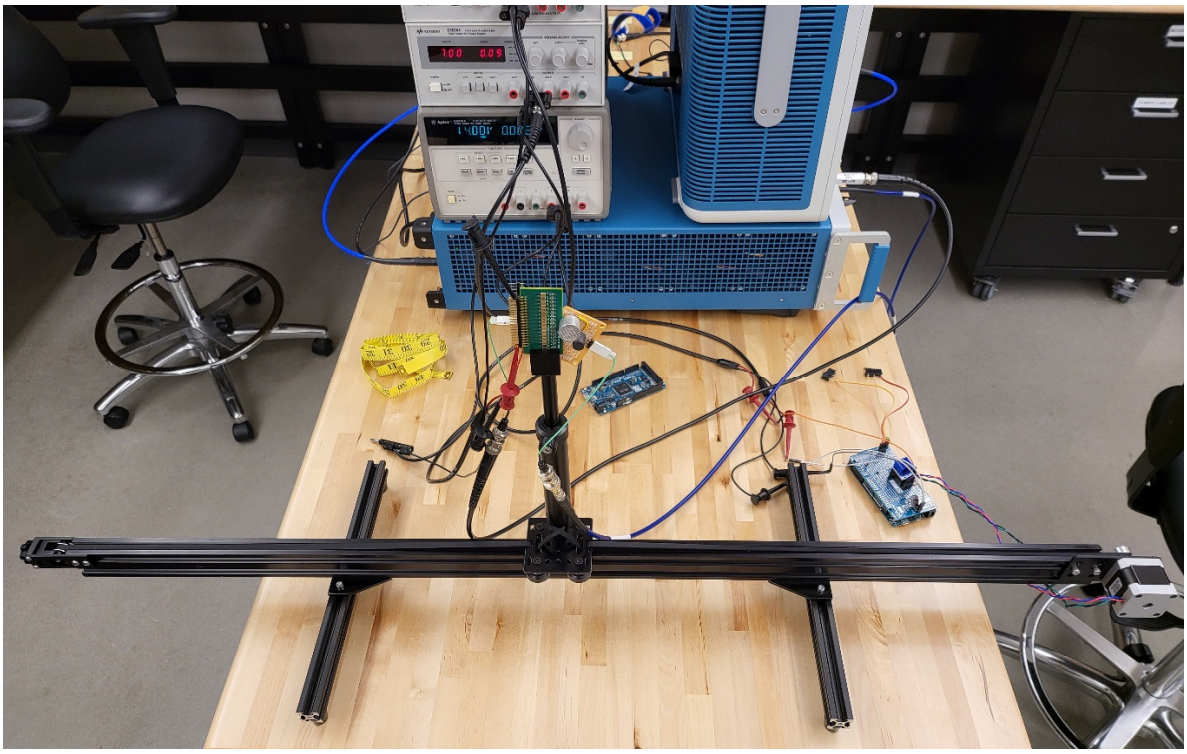

Figure 45: SAR data collection rig

In order to confirm that the new setup was equivalent to the first, the same experiment was preformed again. This collection was length was extended to 40 cm and the step size was reduced to 3.4 mm. After processing the azimuth direction was interpolated down to restore the 2 cm x 2 cm pixels. The raw phase history is shown in Figure 46.

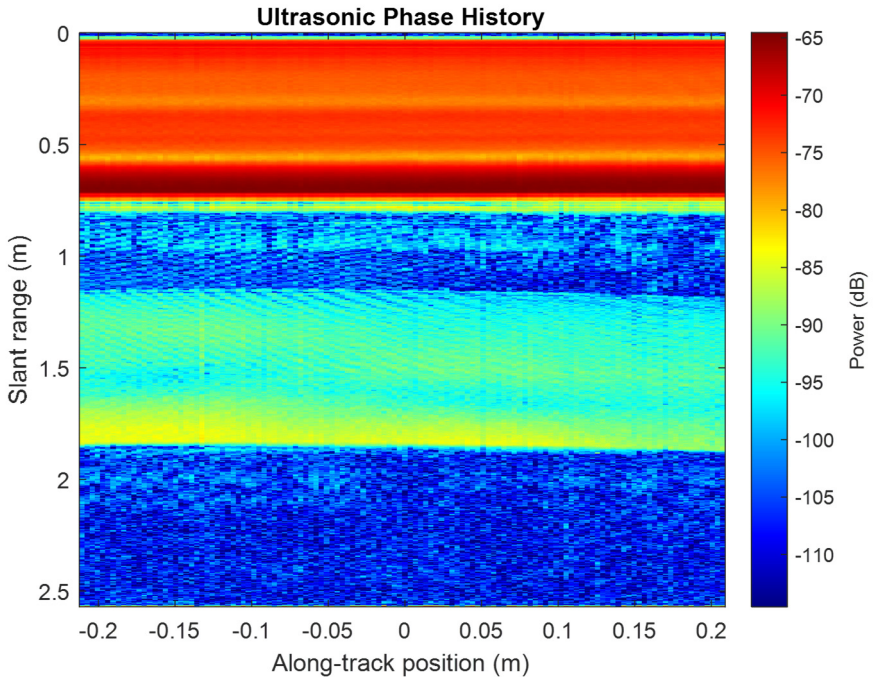

Figure 46: Phase history of second trihedral collection

In accordance with the RDA, this history was pulse compressed down as shown in Figures 47 and 48.

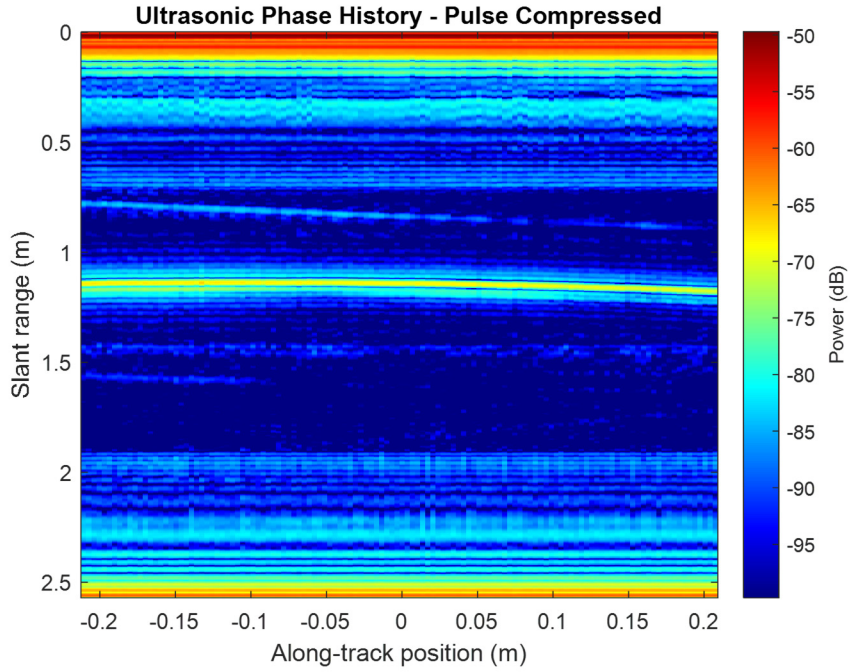

Figure 47: Pulse compressed phase history of second trihedral collection

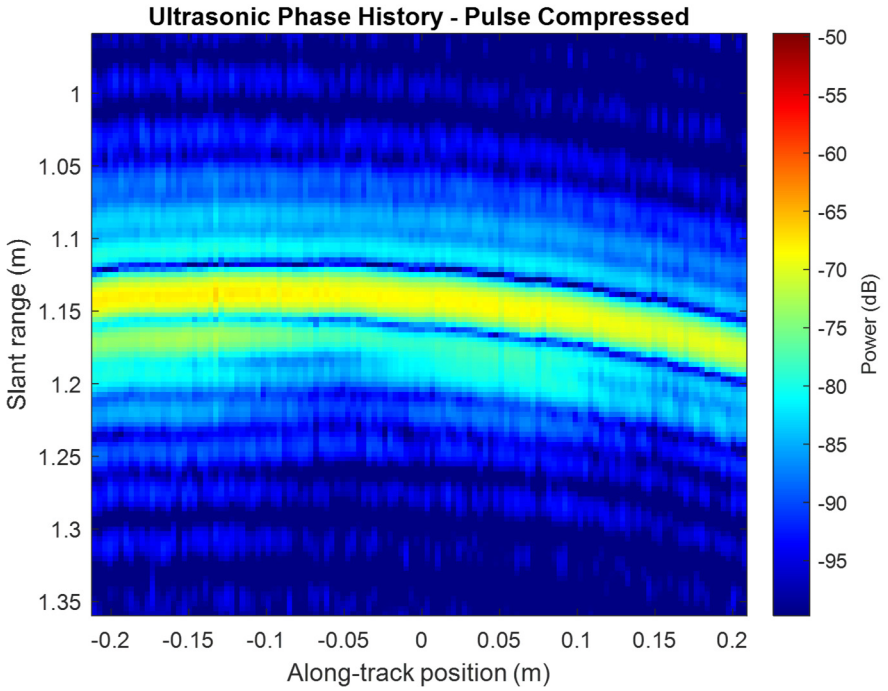

Figure 48: Zoomed in pulse compressed phase history

Since the trach length was much longer, the curve of the object leaving the main lobe of the antenna is evident. The data was then further processed using the RDA to reveal the SAR maps in Figures 49 and 50.

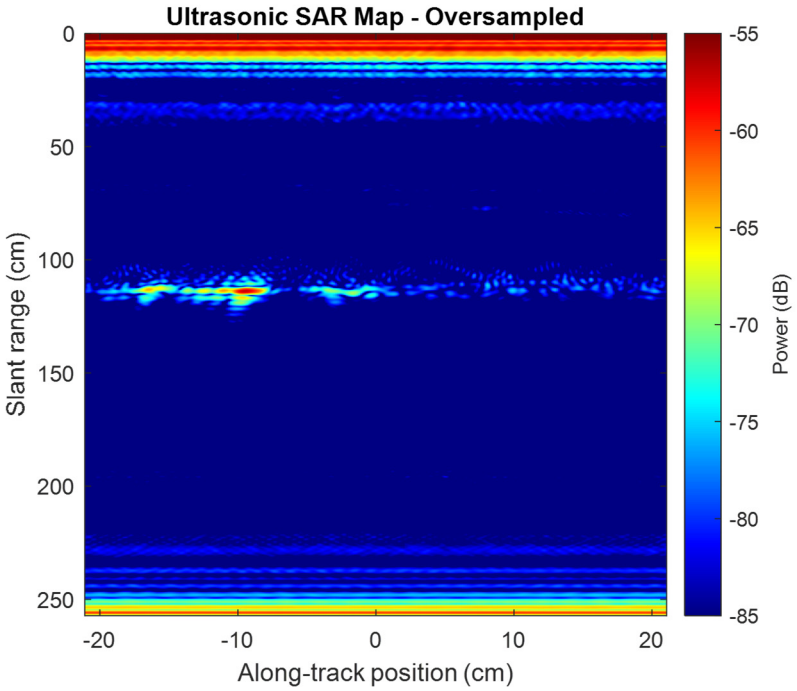

Figure 49: SAR map of second trihedral collection

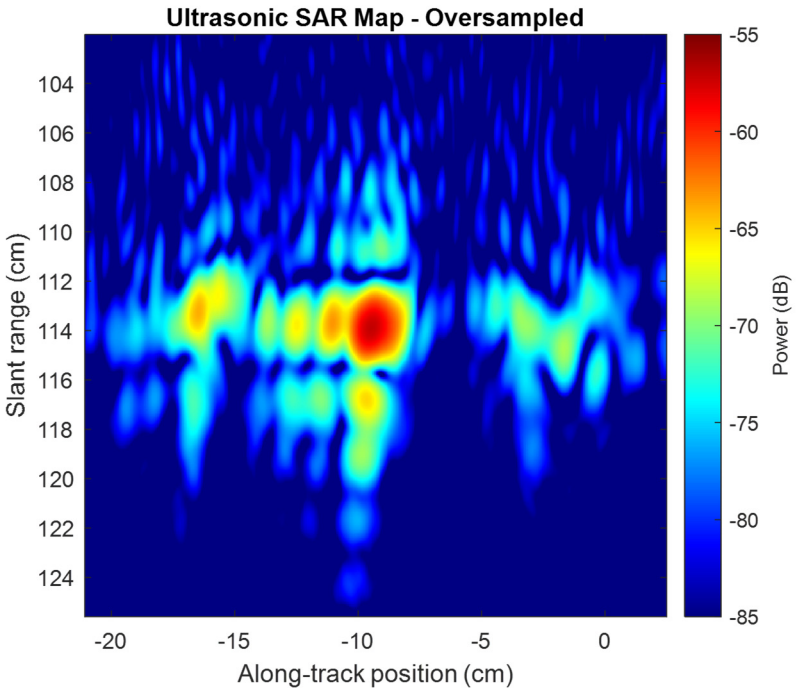

Figure 50: Zoomed in SAR map of the point response

The SAR map shows a clear point response with sidelobes in range and azimuth. There are lobes in azimuth that are ~7 dB down from the main lobe that move when the distance between collections is adjusted. The cause of these lobes is still being investigated.

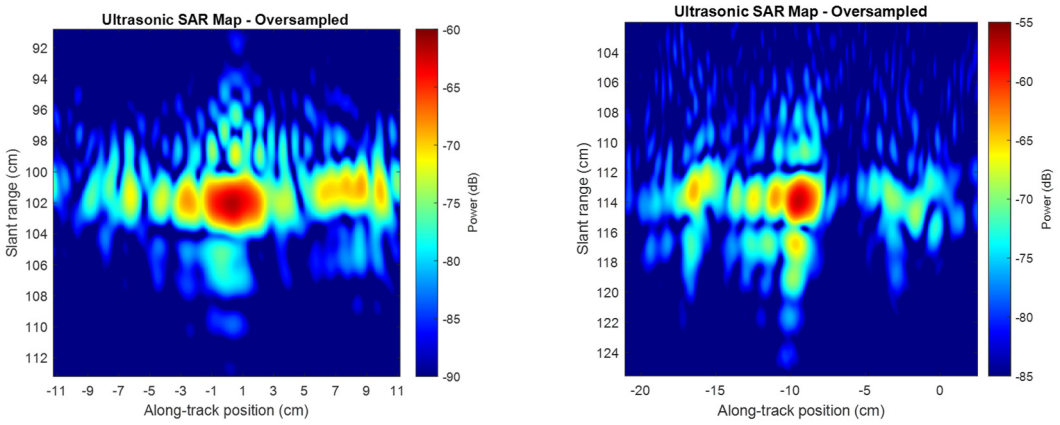

Figure 51: Comparison between first and second trihedral collections

The responses from the first and second trihedral experiments show the same general response. This proved that the new sliding rig was ready for more complex scenes. The complex scene that was imaged was that of a building block comic book car, as seen in Figure 52.

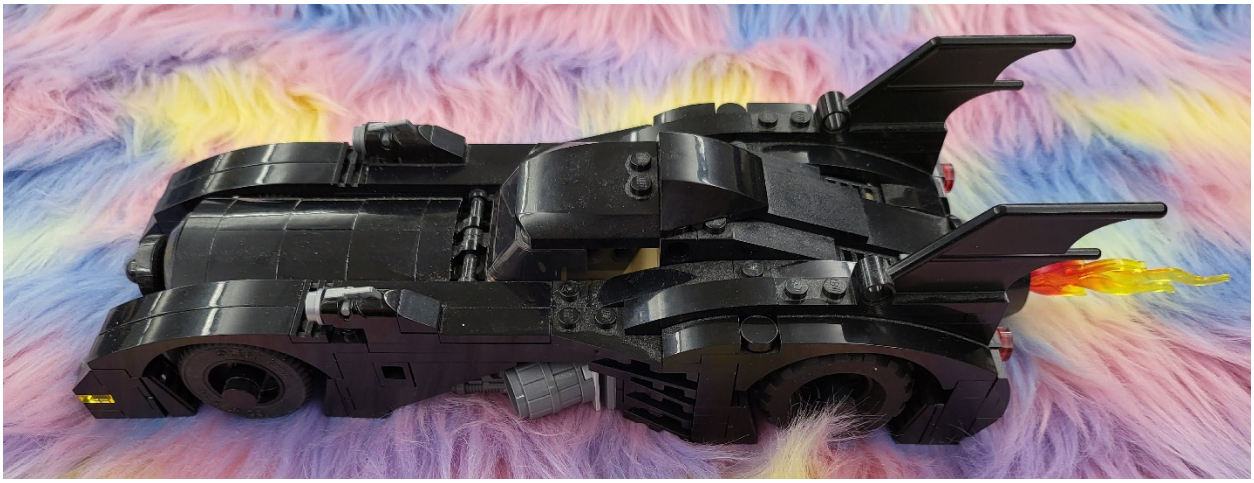

Figure 52: Building block comic book car

The building blocks provided a dense enough material to reflect the acoustic waves, and very precise flat surfaces. The design of the comic book car provided many protrusions from the main body that should show up in a SAR image. The first collection was done with the spacing of 7

mm, the same as the first trihedral experiment. The resulting SAR maps from the RDA are shown in Figures 53 and 54.

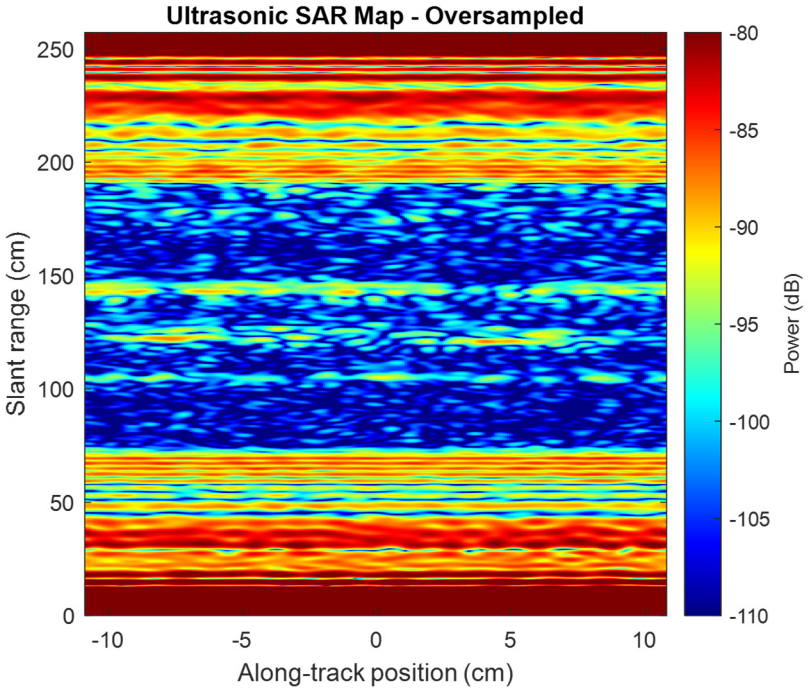

Figure 53: SAR map of the building block comic book car

This SAR map has been flipped vertically compared to the others in order to match how the resulting image would make sense visually. The table edge is seen again around 100 cm. The main return from the object is around 120 cm. The response around 150 cm is from an unknown source. It's doubtful that it is multipath from the complex object, since it is consistently at the same range, and is much too high power. The cause of this return is still under investigation.

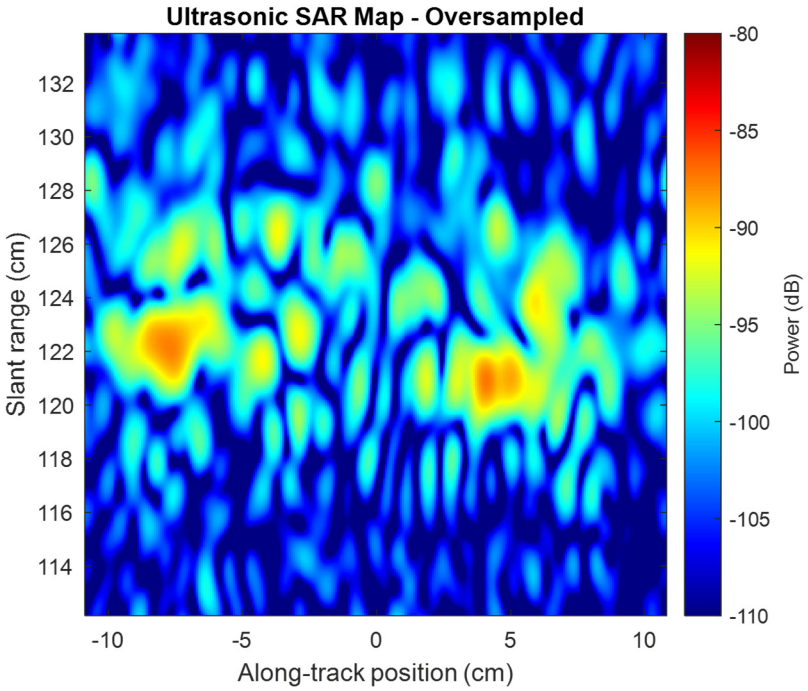

Figure 54: Zoomed in SAR map of the building block comic book car

The main response features a couple of areas with high returns. The left-most one is most likely the front wheel well and the right-most if most likely the rear wheel well. The response near the rear and farther in range could be attributed to the farther fin on the opposite side of the car. A side by side comparison is shown in Figure 55.

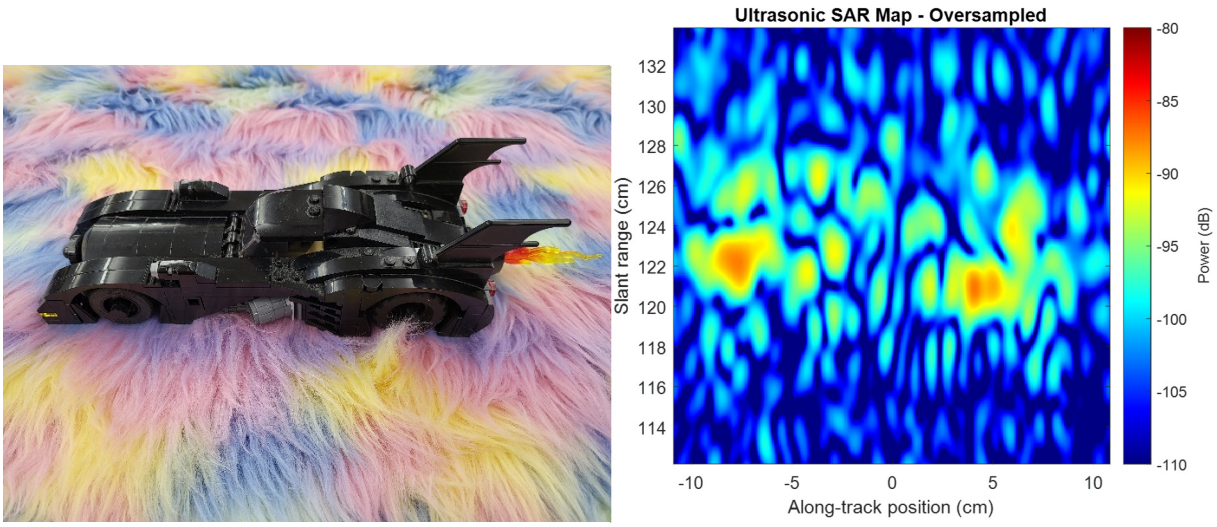

Figure 55: Comparison between object and SAR map

The experiment was run again with the spacing of 3.4 mm, the same as in the second trihedral experiment. This resulted in a higher power return because of the extra energy on the object. The azimuth dimension was the interpolated down to achieve square pixels of 2 cm x 2 cm. The added length of the collection also made it possible to accurately measure the length of the vehicle, which was 24 cm.

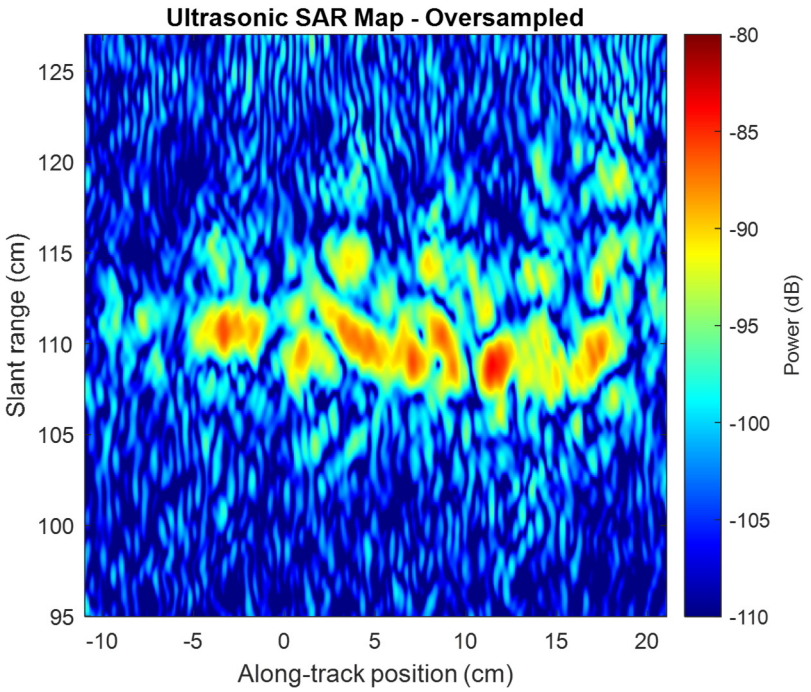

Figure 56: SAR map of second building block comic book car collection

This second collections show the same features as the first, as well as some additional ones due to the increased power. The front and rear wheel wells are again visible, as well as the range displaced return near the rear. A number of the dihedral surfaces on the far edge of the vehicle also exhibit a return. The middle section of the car is much more prominent in this return. A side by side comparison is shown in Figure 57.

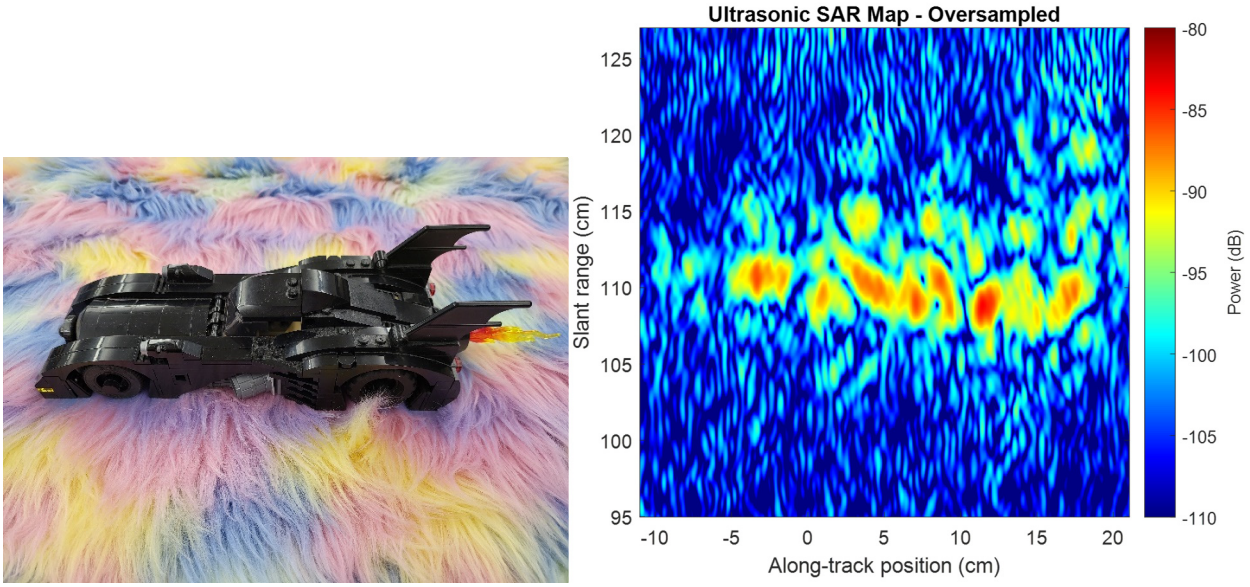

Figure 57: Comparison between object and SAR map

These features are rough due to the pixel size of the SAR image. The comic book car is 12 pixels long and approximately 4 pixels wide. A larger object of the same shape would yield an effectively more detailed response.

5 Conclusions and Future Work

It has been demonstrated that a sodar setup in a laboratory environment can serve as a valuable step between simulation and a complete RF test. The transmitters and receivers are considerably lower cost than those at RF. The quality of the results depends on the collection equipment and processing techniques. In the experiments section it was proved that the fundamentals of radar also apply to the SODAR system. With the advanced radar experiments it was shown that this setup can aid in progressing radar research. Quick iteration times and an easy to use setup allowed for multiple SAR collections that would have taken weeks with an RF system. The SODAR setup also allows for experiments to continue year-round, when outside condition might not permit an RF test.

With the moving rig completed the doors are open for more SAR collections and experiments. The ability to generate SAR phase histories in a lab environment will allow for different waveforms to be used in transmission. The inclusion of a transmission ULA would allow for testing in the areas of spatial diversity and beamforming. Having a transmission and reception ULA would allow for an ultrasonic multiple input multiple output (MIMO) system. MIMO is a hot topic in both radar and comms, and this system could facilitate research in those areas.

6 Works Cited

[1] H. Huang and D. Paramo, "Broadband electrical impedance matching for piezoelectric ultrasound transducers," in *IEEE Transactions on Ultrasonics, Ferroelectrics, and Frequency Control*, vol. 58, no. 12, pp. 2699-2707, December 2011, doi: 10.1109/TUFFC.2011.2132.

[2] C.C. Jones, Z.E. Gannon, D. DePardo, J.W. Owen, S.D. Blunt, C.T. Allen, B.H. Kirk, "*Development & Experimental Assessment of Robust Direction Finding and Self-Calibration*" 2022 IEEE Radar Conference, 2022

[3] I. G. Cumming and F. H.-c. Wong, *Digital processing of synthetic aperture radar data : algorithms and implementation* (Artech House remote sensing library). Boston: Artech House, 2005, pp. xxviii, 625 p.

7 Appendix A – MATLAB Code

This appendix features all the MATLAB code used to generate the figures within this document. The theory figures and pulse compression experiment code were written by me. The direction-finding code was written by Christian Jones. The SAR code section was written by Daniel Herr and includes the preprocessing necessary for the ultrasonic returns to be used in traditional radar processing. This process takes real valued time-domain pass-band signals and converts them to complex baseband. For detailed information see the SAR processing section.

7.1 Theory Figures

```
% Thesis Figures
% Zeus Gannon

%% Theory

% Pulse Length and Bandwidth
fc = 8E+6;
Fs = 100E+6;
Ts = 1/Fs;
FoS = 1;

t_total = -1E-6:Ts:11E-6;

t_one_us = 0:Ts:1E-6;
one_us = [zeros(100,1)' cos(2*pi*fc*t_one_us) zeros(1000,1)'];

t_ten_us = 0:Ts:10E-6;
ten_us = [zeros(100,1)' cos(2*pi*fc*t_ten_us) zeros(100,1)'];

freq = linspace(-Fs/2,Fs/2,length(t_total)*FoS);

one_us_f = fftshift(fft(one_us,length(one_us)*FoS));
one_us_f_norm = one_us_f/max(one_us_f);

ten_us_f = fftshift(fft(ten_us,length(ten_us)*FoS));
ten_us_f_norm = ten_us_f/max(ten_us_f);

figure(1)
subplot(2,2,1)
plot(t_total*1000000,one_us)
axis tight
xlabel("Time (us)")
ylabel("Amplitude (V)")
ylim([-1.1 1.1])
```

```
subplot(2,2,3)
plot(t_total*1000000,ten_us)
axis tight
xlabel("Time (us)")
ylabel("Amplitude (V)")
ylim([-1.1 1.1])

subplot(2,2,2)
plot(freq/1E+6,db(abs(one_us_f_norm)))
xlabel("Frequency (MHz)")
ylabel("Normalized Amplitude (dB)")
xlim([5 11])
ylim([-25 1])

subplot(2,2,4)
plot(freq/1E+6,db(abs(ten_us_f_norm)))
xlabel("Frequency (MHz)")
ylabel("Normalized Amplitude (dB)")
xlim([5 11])
ylim([-25 1])

% Chirped Bandwidth
B = 1E+6;
fs = fc - B;
tau = 10E-6;

s_t = cos(2*pi*(fs*t_ten_us+(B/tau)*t_ten_us.^2));

ten_us_chirp = [zeros((1E-6)/Ts,1)' s_t zeros((1E-6)/Ts,1)'];

% Create signal frequency vector with no zero-padding
s_f = fftshift(fft(s_t, length(s_t) * FoS));
s_f = s_f / max(s_f);
freq_s_t = linspace(-Fs/2,Fs/2,length(s_f));

% Zero-paddding the FFT of the signal causes interpolation in the frequency
% domain. In this case, it causes unwanted ripples.
ten_us_chirp_f = fftshift(fft(ten_us_chirp,length(ten_us_chirp)*FoS));
ten_us_chirp_f_norm = ten_us_chirp_f/max(ten_us_chirp_f);

figure(2)
subplot(1,2,1)
plot(t_total*1000000,ten_us_chirp)
axis tight
xlabel("Time (us)")
ylabel("Amplitude (V)")
ylim([-1.1 1.1])

subplot(1,2,2)
plot(freq_s_t / 1e6,db(abs(s_f)))
xlabel("Frequency (MHz)")
ylabel("Normalized Amplitude (dB)")
xlim([-3 3] + fc / 1e6)
ylim([-40 1])
```

```
% Windowing
B = 50E+6;
fs = 1E+9;
tau = 5e-6;
tVect = -tau/2 : 1/fs : tau/2 - 1/fs;


% window = ones(length(tVect),1)';
% window = hanning(length(tVect))';
window = blackman(length(tVect))';

s = window.*exp(1j*pi*B/tau*tVect.^2);
s = s/norm(s);
mf = flip(conj(s));
NFFT = length(s)+length(mf)-1;
acorr = ifft(fft(s,NFFT).*fft(mf,NFFT));

L = length(acorr);
tLag = 1 / fs * (-floor(L/2) : floor((L-1)/2)).';

figure(3)
subplot(1,2,1)
plot(window)
axis tight
xlabel("Samples")
ylabel("Aplitude")
ylim([0 1.1])

subplot(1,2,2)
plot(tLag/tau,db(acorr))
axis tight
xlabel("Normalized Lag (1/\tau)")
ylabel("Normalized Amplitude (dB)")
xlim([-0.05 0.05])
ylim([-100 0])

% Coherent Averaging

fc = 5e6;
fs = 400e6;
tau = 5e-6;
T = tau * 10;
nAverages = 1000; % Number of Coherent Averages\
n0 = 0.1;

tauVect = (-tau/2 : 1 / fs : tau/2 - 1 / fs).';
tVect = (0 : 1 / fs : T - 1 / fs).';

N = length(tauVect);
M = length(tVect);

% Generate Windowed Gated Sinusoid
s = cos(2 * pi * fc * tauVect);
```

```
s = gausswin(length(s)) .* s;
s = s / norm(s);

s_pad = zeros(M, 1);

iMiddle = round(M/2);

s_pad(iMiddle - N/2 + 1: iMiddle + N/2) = s;

% Simualte AWGN
nMat = n0 * randn(M, nAverages);

yMat = s_pad + nMat;

% Coherent average = 1
y(:,1) = mean(yMat(:,1:1), 2);

% Coherent average = 10
y(:,2) = mean(yMat(:,1:10), 2);

% Coherent average = 100
y(:,3) = mean(yMat(:,1:100), 2);

% Coherent average = 1000
y(:,4) = mean(yMat(:,1:1000), 2);

% Plotting
yLimits = [-0.25 0.25];

figure(4)
subplot(5,1,1)
plot(tVect * 1e6, s_pad,'b');
hold on; grid on;
ylim(yLimits)
text(2, max(yLimits) * 0.7, 'echo only')

subplot(5,1,2)
plot(tVect * 1e6, y(:,1),'r');
hold on; grid on;
plot(tVect * 1e6, s_pad,'b');
ylim(yLimits)
nCoh = 1;
snr = 10 * log10(rms(s) / n0 * sqrt(nCoh));
text(2, max(yLimits) * 0.7, sprintf('echo + noise: Ncoh = %d SNR = %.2f dB',
nCoh, snr))

subplot(5,1,3)
plot(tVect * 1e6, y(:,2),'r');
hold on; grid on;
plot(tVect * 1e6, s_pad,'b');
ylim(yLimits)
nCoh = 10;
snr = 10 * log10(rms(s) / n0 * sqrt(nCoh));
```

```
text(2, max(yLimits) * 0.7, sprintf('echo + noise: Ncoh = %d SNR = %.2f dB',
nCoh, snr))

subplot(5,1,4)
plot(tVect * 1e6, y(:,3),'r');
hold on; grid on;
plot(tVect * 1e6, s_pad,'b');
ylim(yLimits)
nCoh = 100;
snr = 10 * log10(rms(s) / n0 * sqrt(nCoh));
text(2, max(yLimits) * 0.7, sprintf('echo + noise: Ncoh = %d SNR = %.2f dB',
nCoh, snr))

subplot(5,1,5)
plot(tVect * 1e6, y(:,4),'r');
hold on; grid on;
plot(tVect * 1e6, s_pad,'b');
ylim(yLimits)
nCoh = 1000;
snr = 10 * log10(rms(s) / n0 * sqrt(nCoh));
text(2, max(yLimits) * 0.7, sprintf('echo + noise: Ncoh = %d SNR = %.2f dB',
nCoh, snr))
xlabel('Time (\mus)')
```

7.2 Pulse Compression Processing

```
% Pulse Compression Experiment Data Processing
% Zeus Gannon

fc = 40E+3; % Center freq of 40 kHz
Fs = 25E+6; % Sample rate of 25 MS/s

% Extract the Data from the .CSV files
record = readtable('3ms_lfm.csv','NumHeaderLines',2);
loop_back = readtable('3ms_lb.csv','NumHeaderLines',2);
time = table2array(record(:,1));
signal_raw = table2array(record(:,2));
lb_raw = table2array(loop_back(1:2000,2));

% Zero Mean the Loop Back
lb = lb_raw(200:1000) - mean(lb_raw, 1);

% Zero Mean the Response
signal = signal_raw - mean(signal_raw, 1);
signal = signal/max(signal);

% Create a Matched Filter and normalize
mf = flipud(lb);
mf = mf/max(mf);

% Convolve the Matched Filter with the Response
mf_response = conv(signal,mf,'same');
```

```
% Shift the response to compensate for the compression point of the filter
% being in the middle of the waveform instead of the leading edge
mf_response = circshift(mf_response,-310);

% Normalize Match Filtered Response
mf_response_norm = mf_response/max(mf_response);

% Remove Carrier
mf_response_norm_bb = lowpass(mf_response_norm.*sin(2*pi*fc*time),fc,Fs);
mf_response_norm_bb = mf_response_norm_bb/max(abs(mf_response_norm_bb));

figure(1)
plot(time*1000,db(mf_response_norm_bb))
xlabel("Time (ms)")
ylabel("Normalized Magnitude (dB)")
xlim([-2 18])
ylim([-20 2])
```

7.3 Direction Finding Processing with MF and MVDR

```
clear;
clc;
close all;

%% load receive data
% y - MxL matrix of receive measurements where M is number of elements and
% L is number of temporal snapshots

% yn - optional MxLn matrix of quiet receive measurements used to estimate
% the noise covariance where M is number of elements and Ln is number of
% temporal snapshots
%%
M = 8; % number of array elements
MOS = 10; % spatial oversampling ( granularity of plots )

Nsnap = 15; % number of snapshots to use in MVDR assumed to be odd)
N = floor(Nsnap/2);  % 1/2 - 1 number of snapshots we use

fs = 2e3; % receive bandwidth
fc = 40e3; % 40khz center freq
c = 340; % approximate speed of sound, measure this with zeus
lambda = c/fc; % wavelength of center frequency

d = lambda/2; % element spacing
elementd = (0:(M-1)).'-(M-1)/2; % normalized element position vector
% relative to phase center

phi = linspace(-90,90-180/(M*MOS),M*MOS); % spatial angles
S = exp(-1j*2*pi*d/lambda*sind(phi).*(elementd)); % spatial steering vectors

% Rn = yn*yn'/size(yn,2); % data driven noise covariance matrix if available
sign = 0; % estimate noise power in dB
Rn = 10^(sign/10)*eye(M); % estimate noise covariance matrix
```

```
L = size(y,2)-2*N; % number of snapshots after cutting the first and last N
% to ensure MVDR covariance is correct

xmf = zeros(M*MOS,L); % preallocating matched fiter output
xMVDR = zeros(M*MOS,L); % preallocating MVDR output
for mm = 1:L

    ytmp = y(:,mm:(mm+2*N)); % data matrix for this time instance

    % matched fitler
    xmf(:,mm)=S'*ytmp(:,N+1)/M; % matched filter output

    % MVDR
    R = (ytmp*ytmp')/(2*N+1); % form sample covariance matrix
    iRS = (R+Rn)\S; % invert matrix
    W = iRS./sum(conj(S).*iRS,1); % add in MVDR gain constraint
    xMVDR(:,mm) =W'*ytmp(:,N+1); % apply MVDR filter


    disp(num2str(mm/L)) % display how far we are in loop
end
%% element power spectrum
fspace = linspace(fc-fs/2,fs+fs/2,size(y,2));
fspace = fspace/1e3; % convert to kHz
figure(100)
plot(fspace,db(fft(y.')));
xlabel('Frequency (kHz)')
ylabel('Relative Power (dB)')
title('Power spectrum of elements')
%% generate Spatial angle vs Time Images
t = (0:1/fs:(L/fs-1/fs));
t = t/1e-3;% convert to mili seconds
figure(101)
imagesc(t,phi,db(xmf))
% peak normalize color axis by matched fitler output
caxis([max((db(max(abs(xmf).^2,[],2))/2))-30
max((db(max(abs(xmf).^2,[],2))/2))])
title('Time-Angle MF')
xlabel('Time (ms)')
ylabel('Spatial AoA (degrees)')
colorbar
colormap jet
set(gcf,'units','inches')
set(gcf,'position',[5 5 3.5 2.2])

figure(102)
imagesc(t,phi,db(xMVDR))
% peak normalize color axis by matched fitler output
caxis([max((db(max(abs(xmf).^2,[],2))/2))-30
max((db(max(abs(xmf).^2,[],2))/2))])
title(['Time-Angle ',num2str(N*2+1) , ' Snapshot(s) MVDR'])
xlabel('Time (ms)')
ylabel('Spatial AoA (degrees)')
colorbar
```

```
colormap jet
set(gcf,'units','inches')
set(gcf,'position',[5 5 3.5 2.2])
```

7.4 Ultrasonic SAR Processing with Data Conditioning

```
function [dataBbMat] = preprocessUltrasonicData(dataMat, ts, fc, rFactors)
%PREPROCESSULTRASONICDATA Convert passband SAR data to complex baseband
%   Perform complex down-conversion, filtering, and down-sampling to raw SAR
%   data. Returns raw-data in complex baseband form.
%   [dataBbMat] = preprocessUltrasonicData(dataMat, ts, fc, rFactor)
%   dataMat - Data matrix oriented [N_SAMPS N_PRIS]
%   ts      - sample rate (s)
%   fc      - carrier frequency (Hz)
%   rFactor - decimation factors (vector of integers)

[K, N_PULSE] = size(dataMat);
N_RFACTOR = length(rFactors);
downsampleRatio = prod(rFactors);
tVect = (0 : K - 1).' * ts;

% Remove signal mean (from each fast-time collect)
dataMat = dataMat - mean(dataMat, 1);

% Convert to complex baseband
dataMat = hilbert(dataMat);
dataMat = dataMat .* exp(-2j * pi * tVect * fc);

% Filter and downsample each fast-time vector
L = ceil(K / downsampleRatio);
dataBbMat = zeros(L, N_PULSE);  % pre-allocate memory
for iPulse = 1 : N_PULSE

    % Allow decimation in multiple steps to improve performance
    % Not really any differnce at our current configuration
    temp = dataMat(:,iPulse);

    for iFactor = 1 : N_RFACTOR
        r = rFactors(iFactor);
        temp = decimate(temp, r);
    end

    dataBbMat(:,iPulse) = temp;

end

end
```

```
function [sarMapMatMatRangeAzimuth] = rangeDopplerAlgo(rMat, fs, dL, vel, c,
fc, sVect, rangeCenter, tOffset)
%RANGEDOPPLERAGLO Compute SAR map using Range Doppler Algorithm
%   Compresses a raw SAR phase history into a SAR map using the Range
%   Doppler Algorithm. Assumes uniform linear spacing of syntehtic apperture.
%   [sarMapMatMatRangeAzimuth] = rangeDopplerAlgo(rMat, fs, dL, vel, c, fc,
sVect, rangeCenter, tOffset)
%   rMat        - raw SAR phase history orientated [cross-track along-track]
%   fs          - receive sample rate (Hz)
%   dL          - ULA spacing (m)
%   vel         - velocity of platform (m/s) Note: can be set to 1 ->
consider SAR as a phased array problem.
%   c           - velocit of propogation (m/s). For ultrasonic ~ 343 m/s
%   fc          - carrier frequency of radar pulse
%   sVect       - ideal or loopback version of radar pulse. Used for pulse
compression.
%   rangeCenter - center of SAR map. Used as basis for some approximations in
algorithm.
%   tOffset     - time-of-flight value corresponding to first receive sample.
For continous RX, set to 0.



%% Compute setup parameters
[nSampRx, nL] = size(rMat); % phase history dimensions
nSampS = length(sVect); % radar-pulse samples

tPulse = nSampS / fs;   % pulse-duration of radar pulse
ts = 1 / fs;

tDVect = tOffset + (0 : nSampRx - 1).' * ts;    % fast-time delay vector

T = nSampRx / fs;   % fast-time duration of phase-history
dF = 1 / T;         % fast-frequency resolution

T_slow = nL * dL / vel; % slow-time (azimuth) duration of phase-history
dFEtta = 1 / T_slow; % slow-frequency resolution

% Compute phase-history dimension vectors
rDVect = tDVect * c / 2; % Range delay (m)
fTau = ifftshift(-floor(nSampRx / 2) : floor((nSampRx - 1) / 2)).' * dF; %
fast-frequency vector (Hz)
etta = dL / vel * (-floor(nL / 2) : floor((nL - 1) / 2)).'; % slow-time
vector (s)
fEtta = ifftshift(-floor(nL / 2) : floor((nL - 1) / 2)).' * dFEtta; % slow-
frequency vector (Hz)

% % Phase history plotting
% figure()
% imagesc(etta, rDVect, db(rMat))
% caxis([-50 0] + max(max(db(rMat))))
% cb2 = colorbar;
% title('Ultrasonic Phase History')
% ylabel('Slant range (m)')
% xlabel('Along-track position (m)')
```

```
% ylabel(cb2, 'Power (dB)')
% colormap jet

%% Step 1: fft in range
rMatFreqAzimuth = fft(rMat, nSampRx, 1);
%% Note: using nSampRx here causes leading edges of pulse to alias to end of
%        pulse. Consider changing to nfft value computed below.


%% Step 2: pulse-compression
mfVect = flip(conj(sVect)); % generate matched filter
nfft = size(rMat, 1) + size(mfVect, 1) - 1; % number of fft points to avoid
circular convolution effects

% peform matched filtering in frequency domain
mfFreqVect = fft(mfVect, nSampRx, 1);
% pcMatFreqAzimuth = rMatFreqAzimuth .* mfFreqVect;
% pcMatFreqAzimuth = rMatFreqAzimuth .* mfFreqVect .* exp(2j * pi *
fftshift(fTau) * tPulse);
% Adjust for matched filter output to match definition in Cumming and Wong
pcMatFreqAzimuth = rMatFreqAzimuth .* mfFreqVect .* exp(2j * pi *
fftshift(fTau) * (tPulse - 1 / fs));

% % plotting
% pcMatRangeAzimuth = ifft(pcMatFreqAzimuth, nSampRx, 1);

% figure()
% imagesc(etta, rDVect, db(pcMatRangeAzimuth))
% caxis([-50 0] + max(max(db(pcMatRangeAzimuth))))
% cb2 = colorbar;
% title('Ultrasonic Phase History - Pulse Compressed')
% ylabel('Slant range (m)')
% xlabel('Along-track position (m)')
% ylabel(cb2, 'Power (dB)')
% colormap jet



%% Step 3: fft in azimuth
pcMatFreqWavenumber = fft(pcMatFreqAzimuth, nL, 2);



%% Step 3+: perform Secondary Range Compression
vR = vel;
Ro = rangeCenter;
fo = fc;

D = (1 - c^2 * (fEtta.').^2 / (4 * fc^2 * vR^2)) .^ 0.5;
% D = real(D);
% D = D + 0.001;
K_src = 2 * vR^2 * fo^3 * D .^ 3 ./ (c * Ro * (fEtta .').^2);
H_src = exp(-1j * pi * fTau .^ 2 ./ K_src);
```

```
% % Disable SRC
% H_src = ones(size(H_src));

srcMatFreqWavenumber = pcMatFreqWavenumber .* H_src;


% plotting
% pcMatRangeWavenumber = ifft(pcMatFreqWavenumber, nSampRx, 1);
% srcMatRangeWavenumber = ifft(srcMatFreqWavenumber, nSampRx, 1);

% figure()
% imagesc(etta, tDVect * c / 2, db(pcMatRangeWavenumber))
% caxis([-40 0] + max(max(db(pcMatRangeWavenumber))))
% colorbar
% ylim([-0.5 0.5] + rangeCenter)
%
% figure()
% imagesc(etta, tDVect * c / 2, db(srcMatRangeWavenumber))
% caxis([-40 0] + max(max(db(srcMatRangeWavenumber))))
% colorbar
% ylim([-0.5 0.5] + rangeCenter)



%% Step 4: ifft in range

scrMatRangeWavenumber = ifft(srcMatFreqWavenumber, nSampRx, 1);



%% Step 5: range cell migration correction (RCMC)

% Determine range to shift by
rangeCorrection = rDVect * (1 - D) ./ D;


rcmcMatRangeWavenumber = zeros(nSampRx, nL);

for iRange = 1 : nSampRx

    for iAzimuth = 1 : nL

        rangeCorrect = rangeCorrection(iRange, iAzimuth);
        sampCorrect = rangeCorrect * 2 / c * fs;

        % Do the interpolation
        targetSampDelay = iRange + sampCorrect;

%         % Attempt at efficient interpolation
%         intSampDelay = round(targetSampDelay);
%
%         nInterpSide = 4;
%
```

```
%         iInterpPoints = intSampDelay + (-nInterpSide : nInterpSide).';
%
%         interpPoints = scrMatRangeWavenumber(iInterpPoints, iAzimuth);
%
%         myPoint = interp1(1 : length(interpPoints), interpPoints, 1 +
nInterpSide + targetSampDelay - intSampDelay, 'spline');

        % Sinc interpolation
        myPoint = scrMatRangeWavenumber(:,iAzimuth).' * sinc((tDVect -
tOffset - (targetSampDelay - 1) / fs) * fs);

        rcmcMatRangeWavenumber(iRange, iAzimuth) = myPoint;

    end

end

% % plotting
% figure()
% imagesc(fEtta, rDVect, db(srcMatRangeWavenumber))
% caxis([-40 0] + max(max(db(srcMatRangeWavenumber))))
% colorbar
% ylim([-0.5 0.5] + rangeCenter)
%
% figure()
% imagesc(fEtta, rDVect, db(rcmcMatRangeWavenumber))
% caxis([-40 0] + max(max(db(rcmcMatRangeWavenumber))))
% colorbar
% ylim([-0.5 0.5] + rangeCenter)



%% Step 6: azimuth compression

sarMapInterpRA = exp(1j * 4 * pi * rDVect .* D * fc / c);

acMatRangeWavenumber = rcmcMatRangeWavenumber .* sarMapInterpRA;



%% Step 7: Ifft in azimuth

sarMapMatMatRangeAzimuth = ifft(acMatRangeWavenumber, nL, 2);

% % plotting
% figure()
% imagesc([], rDVect, db(sarMapMatMatRangeAzimuth))
% caxis([-40 0] + max(max(db(sarMapMatMatRangeAzimuth))))
% colorbar


%% Step 8: Correct fast-time phase ramp
% Need apply proper phase shift to each range
```

```
% The time-domain correlation method used removes this from the data
sarMapMatMatRangeAzimuth = sarMapMatMatRangeAzimuth .* exp(-2j * pi * fc *
tDVect);


end
```